Phonon-mediated entanglement for trapped ion quantum computing

Phonon-mediated entanglement for trapped ion quantum computing

K-A Brickman Soderberg[1] and C Monroe[2]

[1] Department of Physics, The James Franck Institute, The University of Chicago, Chicago, IL 60637, USA
[2] Joint Quantum Institute, University of Maryland Department of Physics, and National Institute of Standards and Technology, College Park, MD 20742, USA

E-mail: brickman@uchicago.edu

Abstract

Trapped ions are a near ideal system to study quantum information processing due to the high degree of control over the ion's external confinement and internal degrees of freedom. We demonstrate the key steps necessary for trapped ion quantum computing and focus on phonon-mediated entangling gates. We highlight several key algorithms implemented over the last decade with these gates and give a detailed description of Grover's quantum database search implemented with two trapped ion qubits.

(Some figures in this article are in colour only in the electronic version)

This article was invited by Professor J Weiner.

Contents

1. Introduction and brief history of quantum computing

The field of Quantum Information Science (QIS) is a juxtaposition of two great scientific advents of the 20th century: quantum mechanics and information theory. Information theory, beginning with the work of Shannon in 1948, gave mathematical meaning to information in terms of bits, the zeroes and ones that form the basic unit of information [1]. By then, Alan Turing had shown the universality of computing by inventing a theoretical machine that would be able to solve any conceivable mathematical problem—independent of the hardware used [2]. These ideas led to the fruitful search and discovery of electronic switches and transistors, from early vacuum tubes to the modern semiconductor chips that are packed a billion to a square inch. Quantum mechanics was more of a curiosity in the 20th century. Although quantum theory is critical to the fundamental understanding of how objects from molecules to subatomic particles behave, and also for a detailed understanding of certain physical properties (especially at very low temperatures), it still has almost no place in our everyday lives. Conceptually, quantum physics

has a revolutionary basis that allows physical properties to exist in superposition states, with the conventional interpretation that when such states are observed, they collapse into definite states *because of the measurement process*. More than just a curiosity, this attribute is now coming to the forefront in the field of QIS.

Quantum information processors store superpositions of information, most conveniently represented by 'quantum bits' or qubits, which are quantum two-level systems. (Other representations are possible, but are not covered in this paper.) When N qubits are considered, the most general quantum state carries an amount of information that is exponential in N, in the sense that there are $2^N - 1$ independent complex numbers required to represent the state. Such states generally also carry entanglement, which is a central concept in QIS, and is thought to be the source of the power of quantum computing [3].

Richard Feynman inspired many of the early ideas in QIS in the context of quantum simulations [4], where a collection of qubits is engineered to evolve according to a given Hamiltonian through the application of external control fields. Feynman was motivated by the difficulty in integrating the Schrödinger equation in typical Hamiltonian systems, owing to the exponential growth in Hilbert space as the system becomes large. He proposed that a controllable system of qubits would be able to efficiently simulate the given Hamiltonian. In the 1980s, David Deutsch proposed the use of qubits to solve certain toy problems that could not be solved classically. For instance, there are four possible single-bit functions $f(x)$ of a single-bit input x: $f(x) = 0, 1, x, \bar{x}$. The first two are termed 'constant' and the last two 'balanced'. Classically, two evaluations of $f(x)$ are required to determine whether the function is constant or balanced. In the quantum realm, the Deutsch–Jozsa algorithm shows how to do this with just a single function evaluation, exploiting the use of superpositions of inputs [5, 6]. In 1994, Peter Shor applied qubits to the problem of number factorization, showing an algorithm that could potentially factor numbers exponentially faster than any known classical algorithm [7]. This application remains the most important application of quantum computers, although there are several other quantum algorithms that have been uncovered.

One key difference between classical and quantum computing is the fragility of quantum states and the apparent inability to apply direct feedback and cause quantum states to latch. Because quantum states are defined by continuous-variable state amplitudes, errors generally accumulate, similar to the case for analog computational devices. Thus it was very significant when in the late 1990s it was discovered that qubits can also latch and be stabilized through the use of quantum error correction [8, 9]. Similar to their classical counterpart, quantum error correction uses an expanded set of qubits and a redundant encoding scheme to recover from qubit errors. Of course the process of encoding/decoding can itself have significant errors, so an important theoretical result was the proof of the existence of fault-tolerant quantum error correction thresholds [10]. As long as the error rate of any quantum operation is below a threshold, arbitrary-length quantum computation can proceed. While the redundancy

overhead in extra qubits and time (and the required level of errors to meet the threshold) are stringent, quantum hardware may someday advance to the stage where quantum computing becomes stable.

Trapped atomic ions are a strong candidate for QIS hardware due to the high degree of control over both internal and external atomic degrees of freedom. Often the challenge in QIS is to find a system that is decoupled from the environment during the quantum operations, but that can also be be strongly coupled to the environment for readout purposes. Trapped ions allow for both of these possibilities. Unwanted coupling to the environment is suppressed by electromagnetically trapping the ions and housing them in vacuum chambers at pressures around 10^{-12} Torr. These ultrahigh vacuum conditions considerably reduce the possibility of background collisions. However, using light near resonant with an atomic transition allows for extremely strong coupling to the environment for readout purposes. In addition, the ions can be very strongly coupled to each other through the collective motional mode resulting from the Coloumb interaction. But, this motion can also be quenched when it is not necessary.

Trapped ion QIS got its start in the mid-1990s when Cirac and Zoller first proposed to use the collective Coulomb motion of an ion crystal to entangle the spins states of individual ions [11]. Later that same year, researchers at the National Institute of Standards and Technology (NIST) demonstrated the first trapped ion entangling gate [12]. Since the first entangling gate demonstration the field has dramatically progressed and is now among the leading candidates to realize a scalable quantum computer capable of performing more than just trivial calculations.

This paper will present a brief review of some of the work done in trapped ion quantum computing over the last decade. Specifically we will focus on phonon-mediated entangling gates. In the second section we will present the necessary requirements to realize a scalable quantum computer and define common terms that will be used throughout the text. The third section will describe the basics of ion trapping and how to perform various qubit operations with trapped ions. The fourth section will detail the common entangling gate schemes and highlight some of the few qubit algorithms that have been implemented. We will conclude with this work being done on state-of-the-art ion trap designs and give a general outlook for the future of the field.

2. General quantum computing terminology and necessary requirements

The conventional architecture for quantum computing is the circuit model [3]. This model consists of a series of wires representing individual qubits and gates to perform qubit manipulations. Gates that are confined to one wire represent single qubit rotations while gates that span more than one wire represent entangling operations. There are several apparent requirements for scalable quantum computer hardware [13]:

(i) A scalable physical system with well characterized qubits,
(ii) The ability to initialize the state to a well-known value,

Table 1. Truth table for both single and multi-bit classical and quantum gates. The classical operations shown are the NOT gate and the two bit AND gate. The NOT gate is a bit flip operation and the corresponding quantum gate is a single qubit rotation. Unlike the NOT gate the single qubit rotation can make an arbitrary superposition of $\alpha|0\rangle + \beta|1\rangle$. The two bit AND gate results in a '1' output only if the two input bits are in the '1' state. Its quantum counterpart is the CNOT gate whose action is to flip the state of the target (second) bit if the control (first) bit is in the $|1\rangle$ state.

	Classical	Quantum
single-bit operations	NOT gate	single-qubit rotation
	$0 \rightarrow 1$	$|0\rangle \rightarrow \cos\left(\frac{\theta}{2}\right)|0\rangle + e^{i\phi}\sin\left(\frac{\theta}{2}\right)|1\rangle$
	$1 \rightarrow 0$	$|1\rangle \rightarrow \cos\left(\frac{\theta}{2}\right)|1\rangle - e^{-i\phi}\sin\left(\frac{\theta}{2}\right)|0\rangle$
2 bit operations	2 bit AND gate	2 qubit controlled-NOT (CNOT)
	$00 \rightarrow 0$	$|00\rangle \rightarrow |00\rangle$
	$01 \rightarrow 0$	$|01\rangle \rightarrow |01\rangle$
	$10 \rightarrow 0$	$|10\rangle \rightarrow |11\rangle$
	$11 \rightarrow 1$	$|11\rangle \rightarrow |10\rangle$

(iii) Long relevant decoherence times, much longer than gate operation time,

(iv) A universal set of quantum gates and

(v) A qubit-specific measurement capability.

All of these criteria have been met in trapped ion systems [14, 15], and the biggest remaining challenge is to scale this system to a nontrivial number of qubits. In the sections that follow, we summarize the demonstrations of the above criteria in various trapped ion experiments.

The first criterion is to identify a set of qubits in which to store information, and throughout we will define these qubit levels as $|0\rangle$ and $|1\rangle$. Any two-level system can serve as a qubit but the two levels must be distinguishable in order to read them out. Additionally, one needs the ability to prepare the qubits in a well-known initial state and the qubit coherence time needs to be much longer than the qubit operation time so that the information is not lost before the readout operation is performed.

A universal quantum gate family can consist of both single qubit and nearly any multiqubit entangling gate. Table 1 outlines two particular types of gates and gives examples of their classical counterparts. In classical computing, the only nontrivial single-bit gate is the NOT operation or a bit flip. The quantum computing analog to this gate is a single qubit rotation that can not only perform a bit flip, but also can create an arbitrary superposition of the qubit basis states $\alpha|0\rangle + \beta|1\rangle$, where $|\alpha|^2 + |\beta|^2 = 1$. A convenient representation of single qubit rotations is evolution on the Bloch sphere. This is a unit sphere where the state of the qubit is defined by two Euler angles θ and ϕ as $\cos(\frac{\theta}{2})|0\rangle + e^{i\phi}\sin(\frac{\theta}{2})|1\rangle$, as shown in figure 1.

Multiqubit entangling operations are critical to quantum computing. Table 1 shows a classical two-bit AND gate and a two qubit quantum controlled-NOT (CNOT) gate. The AND gate returns an '1' output if and only if the two input states are also in the '1' state. Similarly the quantum CNOT operation has the effect of flipping the second (target) bit if and only if the first (control) bit is high, but this gate is much richer than its classical counterpart as it allows the creation of entangled superpositions. Applying this gate two qubits, $q1$ and $q2$, initially prepared in the superposition
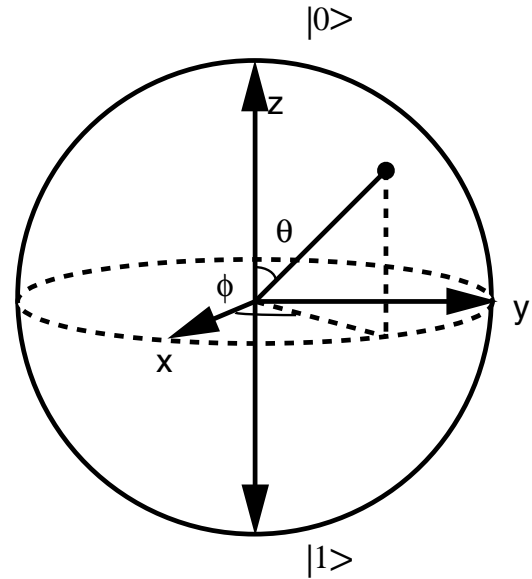

Figure 1. Representation of the Bloch sphere. The positive z-direction represents the $|0\rangle$ state and the negative z-direction represents the $|1\rangle$ state. Rotations by $R(\theta, \varphi)$ dictate how the qubit state evolves while undergoing qubit rotations.

state $|0 + 1\rangle_{q1}|0\rangle_{q2}$ yields the outcome $|00 + 11\rangle$, which is an entangled state that can no longer be written as a product state. Entanglement is defined mathematically as a state that cannot be factored into a product of its constituent parts.

A common characterization of entanglement is the overlap fidelity $F = \langle\Psi|\rho|\Psi\rangle$ between a given state ρ and a particular target entangled state Ψ. To prove entanglement, the fidelity with respect to a given entangled state must be greater than 0.5. Although the fidelity is a quick way to see if a state is entangled without measuring the entire density matrix, it depends upon the target state. There are many other more general indicators of entanglement, including 'negativity,' entanglement of formation and concurrence [16–21].

The above entanglement measures can usually be related to the mean success of an algorithm, but another interesting quantity to consider is the information content of qubit
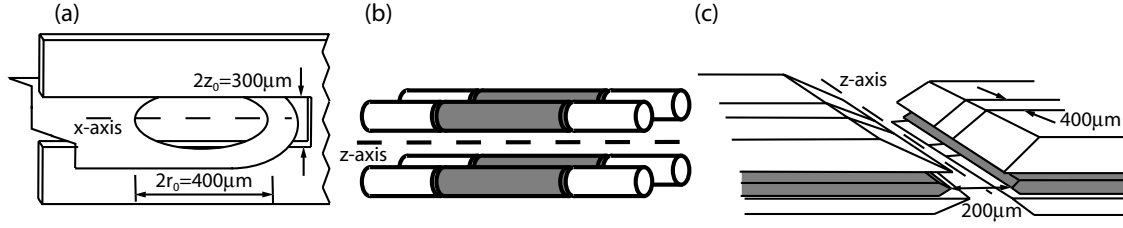
Figure 2. Three common ion trap geometries. (*a*) Representation of an asymmetric 3D quadrapole ring and fork trap. This trap results in a trapping node in a single point in space. (*b*) Schematic of a four rod linear ion trap with one pair of diagonal rods carrying rf potential with respect to the other pair. This trapping geometry results in a linear trapping node which makes it easier to manipulate the ions with focused laser beams. (*c*) A three-layer linear trap (gray-shaded electrodes carry rf potential). This trapping potential is nearly identical to the four rod trap but the three-layer geometry allows one to cancel stray electric fields in any direction.

value distributions. This can be characterized by the mutual information, which measures how much information the two random variables, x and y, have in common. It is defined by $H(x : y) = H(x) + H(y) - H(x, y)$, where $H(x, y) = -\sum_{x,y} p(x, y) \log_2 p(x, y)$ is the joint-Shannon entropy between the two distributions, $p(x, y) = p(x)p(y|x)$ is the joint-probability distribution of x and y, and $p(y|x)$ is the conditional probability of y given that x was measured. $H(x) = -\sum_x p(x) \log_2 p(x)$ and $H(y) = -\sum_y p(y) \log_2 p(y)$ are the Shannon entropies of the individual variables [3].

One last concept to discuss is decoherence or quantum noise. Decoherence leads to unwanted changes in the state of the qubit and in the context of trapped ions can come from many sources including electric field noise leading to motional heating, magnetic field noise and collisions with other atoms. If the decoherence in a system is too large or the decoherence rate occurs faster than the gate operation times, then the quantum information will be lost. The use of quantum error correction encoding with an expanded number of qubits can help mitigate the effects of decoherence [3], but this is only effective when noise levels are below certain thresholds. As will be discussed later in the paper, decoherence is an increasingly important issue as the ion trap designs become more complex.

3. Trapped ions

A quantum computer requires qubits that couple strongly to each other but weakly to the environment during the computation, yet couple strongly to the environment when measured. A system of trapped atomic ions confined in a radio frequency(rf) Paul trap is a near ideal system to satisfy these requirements due to the tight confinement possible in these traps, the strong interactions between ions due to their Coulomb repulsion, and the high level of control possible with laser and microwave fields [22, 23]. Work carried out over the last decade has proven that trapped ions are a compelling quantum computer architecture.

3.1. The rf-Paul trap

All ion trap based quantum computing experiments have dealt with rf-Paul traps, which employ an electric quadrapole field with an oscillating rf potential [24, 25]. The oscillating

field results in a ponderomotive pseudopotential of the form $\Psi(x, y, z) = (m/2)(\omega_x^2 x^2 + \omega_y^2 y^2 + \omega_z^2 z^2)$, where ω_x, ω_y and ω_z are the effective harmonic oscillation frequencies in the x, y and z directions and m is the mass of the ion. In the following derivations we will work in the pseudopotential approximation where we assume that the oscillation frequency of the ion is much less than the rf driving field $\omega \ll \Omega_{rf}$ [26]. In addition, we assume that the traps discussed below operate in a stable trapping region [27].

The simplest ion trap is a symmetric 3D quadrapole trap that consists of a ring electrode surrounded by hyperbolic electrodes which results in a quadrapole field of the exact form $V(x, y, z, t) = (U_0 + V_0 \cos(\Omega_{rf}t))[1/2 - (x^2 + y^2 - 2z^2)/d^2]$. Here V_0 is the radiofrequency (rf) voltage amplitude, Ω_{rf} is the rf drive frequency, U_0 is a static voltage across the electrodes and $d = r_0^2 + 2z_e^2$ is the characteristic size of the trap with r_0 the radius of the ring electrode and $2z_e$ the distance between the two endcaps. This potential results in a single rf node at the trap center. A variation of this trap is shown in figure 2. It is called a 'ring and fork trap' as it is comprised a ring electrode surrounded by a fork electrode. To lowest order, the resulting field is similar to that of the ideal hyperbolic geometry but with some modifications due to the asymmetry arising from the fork electrode [28].

The 3D rf-quadrapole traps are not ideal for quantum information studies because there is only a single point in space where the rf fields vanish. For more than one ion, there is a high level of induced rf 'micromotion' that can hinder the control of the motion of the ion crystal. For many ions, it is difficult to laser cool the ions sufficiently to form a stationary crystal. A more suitable geometry is for the ions to lie along a linear rf node. This can be accomplished with a linear trap consisting of hybrid rf and static potentials as shown in figure 2(*b*). The trap in the figure consists of four rods segmented into 12 electrodes. A potential of $V_0 \cos(\Omega_{rf}t) + U_t$ is applied to two opposing inner diagonal electrodes, here V_0 and U_t are the transverse rf and static voltages, and the other two inner electrodes are grounded. A static voltage U_0 is applied to the outer electrodes, serving as endcaps to confine the ions in the z-direction.

Near the axis of the trap, the potential due to the confining endcaps is

$$V_{static}(x, y, z) = \frac{\kappa U_0}{z_e^2}[2z^2 - x^2 - y^2]$$
$$= (m\omega_z^2/2e)[2z^2 - x^2 - y^2]. \quad (1)$$

Here κ is a dimensionless geometric factor of order unity, $\omega_z = \sqrt{(2eU_0\kappa)/(mz_e^2)}$ is the longitudinal trap frequency and e is the charge of the electron. This static potential results in an anti-trap along the transverse directions x and y, but the pondermotive rf potential easily overwhelms this anti-trapping effect from the static voltage. The potential from the voltages applied to the inner electrodes is

$$V_t(x, y) = \frac{\beta}{2}(V_0 \cos(\Omega_{rf}t) + U_t)\left(1 + \frac{x^2 - y^2}{R^2}\right), \quad (2)$$

where β is a geometric factor, V_0 and U_t are the applied transverse rf and static voltages and R is the distance from the trap center to the nearest electrode. This gives transverse trapping frequencies of

$$\omega_{x,y} = \sqrt{\left(\frac{\beta e V_0}{\sqrt{2}m\Omega_{rf}R^2}\right)^2 - \frac{\kappa e U_0}{mz_0^2} \pm \frac{\beta e U_t}{mR^2}}, \quad (3)$$

where $\pm$ denotes the x and y directions, respectively. The U_t term is important to break the symmetry in the x and y directions so there are well-defined transverse principle axes of motion [29].

Given the above potentials, the equations of motion governing the ion are

$$\frac{d^2x}{d\tau^2} + (a + 2q\cos(2\tau))x = \frac{eE_x^{(0)}}{m},$$

$$\frac{d^2y}{d\tau^2} + (a + 2q\cos(2\tau))y = \frac{eE_y^{(0)}}{m}, \quad (4)$$

$$\frac{d^2z}{d\tau^2} + (2a + 4q\cos(2\tau))z = \frac{eE_z^{(0)}}{m}.$$

Here $\tau = (1/2)\Omega_{rf}t$, $a = 8eU_0/m\Omega_{rf}^2 R^2$, $q = 4eV_0/m\Omega_{rf}^2 R^2$ and $\boldsymbol{E^{(0)}}$ is a stray uniform electric field term (ideally set to zero). The ion dynamics are given by the following equation where, for simplicity, we have focused on only the solution in the x-direction,

$$x(t) = x_0 \cos(\omega_x t)\left[1 - \frac{q}{2}\cos(\Omega_{rf}t)\right] + \frac{eE_x^{(0)}}{m\omega_x^2}$$

$$+ \frac{\sqrt{2}eE_x^{(0)}}{m\omega_x\Omega_{rf}}\cos(\Omega_{rf}t). \quad (5)$$

Equation (5) contains four parts: a secular frequency oscillating at ω_x, a faster micromotion component oscillating near the rf drive frequency $\Omega_{rf} \pm \omega_x$ and two terms describing the dynamics in the presence of an offset field $E_x^{(0)}$. The first two terms correspond to the solution one would get by setting equations (4) equal to zero, a secular frequency term and a micromotion term. If we assume that $a \ll q^2 \ll 1$ and $U_0 \approx 0$, then the micromotion term oscillating at the rf drive frequency is suppressed by a factor of $q/2$ compared with the secular motion and can be neglected. In this case, the motion of the ion is well approximated as a simple harmonic oscillator with oscillation frequency ω_x. The last two terms in equation (5) arise from a stray offset field $E_x^{(0)}$ that may be present in the vicinity of the ion. The third term in equation (5)

represents an offset of the ion position away from the rf zero. The fourth term is a component driven at Ω_{rf} which leads to excess micromotion in the ion. This micromotion differs from the micromotion present in the second term, in that it is a driven motion proportional to the background electric field $E_x^{(0)}$. This motion can inhibit laser cooling due to excess Doppler broadening of the spectrum, so it is important to cancel this term by applying additional static voltages to the trap electrodes.

In practice, the geometry of the linear traps may look different than the four rod trap described above, but the physics is identical. Most of the work in this paper was carried out in some form of a three-layer rf-linear trap, an example of which is shown in figure 2(c) [30]. The three-layer trap is advantageous because it allows compensation of stray offset fields in any direction without floating the rf electrode.

3.2. Hyperfine and optical electronic qubit levels within an ion

Popular ions to use for quantum computing include the alkaline-like atoms Be$^+$, Mg$^+$, Zn$^+$, Cd$^+$, Hg$^+$, Yb$^+$, Ca$^+$, Sr$^+$ and Ba$^+$. These ions can be broken up into two classes: one with a closed transition from the ground state through the excited P state (Be$^+$, Mg$^+$, Zn$^+$, Cd$^+$, Hg$^+$, Yb$^+$) and ones that do not have a closed transition from one of the qubit levels through the excited P state (Ca$^+$, Sr$^+$, Ba$^+$). For the latter group, a low lying metastable D state is often utilized for certain qubit operations, as will be discussed below.

For most of the species listed above the qubit levels consist of the odd isotope (nuclear spinful) $S_{1/2}$ ground state hyperfine levels. These are commonly referred to as hyperfine qubits and the transitions occur in the gigahertz frequency range. The states make near ideal qubits because they are long lived and the large hyperfine splittings allow for near perfect detection efficiencies. In addition, the low lying electronic states allow for the possibility of optical transitions between the hyperfine states. For the closed transition elements direct detection between the qubit levels is possible, but for the open transition elements other techniques, such as shelving one of the qubit levels to a different state or rapid adiabatic passage, must be employed for efficient detection [31–34].

For ions lacking hyperfine structure (even isotopes) another alternative for qubit levels is to use a ground state and a metastable orbital electronic state, as is done in ^{40}Ca$^+$ [35, 36]. Since this transition lies in the optical frequency regime, these are referred to as optical qubits. Optical qubits have a shorter lifetime than hyperfine qubits due to spontaneous emission, but they can be detected with higher efficiencies because of the larger qubit splittings.

The rest of this section will focus on the ^{111}Cd$^+$ ion, which has the simplest atomic structure of all of the elements listed above. Figure 3 shows the energy levels for ^{111}Cd$^+$. The ground state hyperfine levels, $S_{1/2}|F = 0, m_f = 0\rangle = |0\rangle = |\uparrow\rangle$, $S_{1/2}|F = 1, m_f = 0\rangle = |1\rangle = |\downarrow\rangle$ serve as qubit states. These states make ideal qubits due to the long lifetimes, the magnetic field insensitivity to first order, and the large hyperfine splitting of $\omega_{HF}/2\pi = 14.5$ GHz allows for near
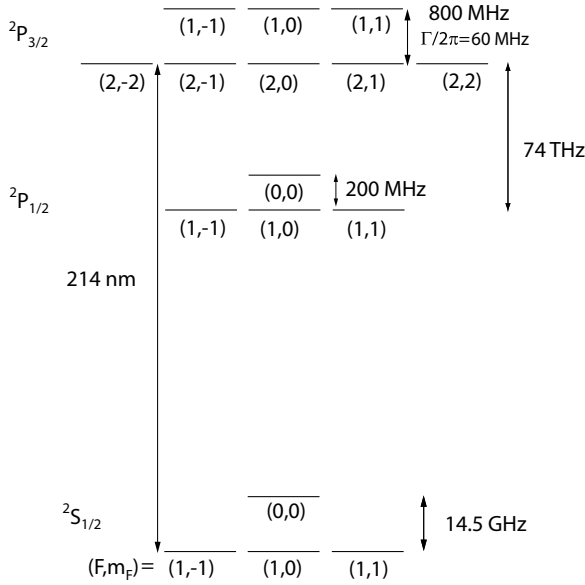
Figure 3. Energy level diagram of $^{111}\text{Cd}^+$. The ground state hyperfine levels serve as qubits and are defined as $S_{1/2}|F=0, m_f=0\rangle = |0\rangle$ and $S_{1/2}|F=1, m_f=0\rangle = |1\rangle$. The large hyperfine splitting of $\omega_{HF}/2\pi = 14.5\,\text{GHz}$ allows for near perfect detection efficiency between the two qubit levels. In addition, the large fine structure splitting of $\Delta_{FS}/2\pi = 74\,\text{THz}$ allows for a large laser detunings during certain qubit operations, such as stimulated Raman transitions, which results in lower spontaneous emission rates.

perfect detection efficiency between the two qubit states. The level structure is considerably simplified in $^{111}\text{Cd}^+$ due to its spin 1/2 nucleus. This makes operations such as optical pumping very efficient since there are at most three levels involved in the ground state and four involved in the excited state. Qubit manipulation is focused on the $^2S_{1/2} \rightarrow {}^2P_{3/2}$ transition, and the absence of a low lying D state reduces the number of lasers necessary since there is no need for a repumping laser as in other systems such as Ca⁺, Sr⁺, Ba⁺ and Yb⁺.

3.3. Measuring the quantum state of trapped ion qubits

Two important requirements for quantum computing are the ability to initialize the system and to have a qubit-specific measurement capability. Both of these steps are illustrated in figure 4(a). Initialization is accomplished with near perfect efficiency by applying π-polarized light tuned to the $^2S_{1/2}|F=1\rangle \rightarrow {}^2P_{3/2}|F=1\rangle$ transition, this optically pumps any population in the $^2S_{1/2}|F=1\rangle$ states to the $^2S_{1/2}|F=0\rangle$ state. Measurement, or detection, of the ions is accomplished via σ^+ polarized light resonant with the $^2S_{1/2} \rightarrow {}^2P_{3/2}$ transition. Any population in the $|1\rangle$ qubit state is optically pumped to the $^2P_{3/2}|F=2, m_f=2\rangle$ state where it undergoes a cycling transition. Since this is a resonant process, a large number of photons are scattered and this state is called the 'bright' state. On the other hand, if this same resonant light is applied to the ions when the population is in the $|0\rangle$ qubit state, very few photons are scattered since the light is now roughly 14 GHz off resonance and so this is referred to as the 'dark'

state. The light can be collected on a photon multiplier tube (PMT) or imaged on to a charge coupled device (CCD) camera for measurement.

The counts from a single ion can be binned as shown in the histogram of figure 5. Using this detection scheme we are able to detect the state of a single $^{111}\text{Cd}^+$ ion with 99.7% efficiency using a PMT [37]. For the case of detecting two ions simultaneously the overall detection fidelity decreases since there are four possible states: both ions bright, bright/dark+dark/bright and both ions dark. In order to achieve good detection fidelity in this case, the three distributions must be well separated so that there is a divide between the bright/dark+dark/bright, and bright/bright case, as shown in figure 6. The maximum detection fidelity for two $^{111}\text{Cd}^+$ ions measured using a PMT is 97%. However, detection fidelities of greater than 98% are possible for two ions using a CCD camera, CCD cameras are also advantageous to use when spatial information about the ions is required [37].

3.4. Laser cooling of motion to make use of Coulomb interaction

Ions confined in a linear rf-Paul trap share a collective motional mode due to their Coulomb repulsion. This motional mode can be used as a bus to transfer information between the ions. However, in order to use this motional mode as a databus, one must first cool the ions to near the motional ground state. For all of the quantum operations discussed in the rest of the paper, the ions must be kept within the Lamb–Dicke limit (LDL). In this regime the extent of the ions wavepacket is much less than that of the exciting light and is defined by $\eta\sqrt{\bar{n}+1} \ll 1$. Here $\eta = k_z z_0$ is Lamb–Dicke parameter, $k_z = k\cdot\vec{z}$ is the component of the wavevector in the z-direction, and $z_0 = \sqrt{\hbar/(2m\omega_z)}$ is the spread of the ion's wavepacket in the ground state.

Another advantageous aspect of the motional mode is that it allows thermometry to be carried out on the ions. The intensity of the ions' sideband spectrum is a 'temperature' gauge in the system. The average vibrational level, $\bar{n}$, occupied by the ion can be deduced from the ratio of the red to the blue sideband transition probabilities by $P_{bsb}(0)/P_{rsb}(0) = \bar{n}/(1+\bar{n})$. A red sideband drives a transition that increases the motional state by $|n+1\rangle$ quanta, while a blue sideband drives a transition that decreases the motional state by $|n-1\rangle$ quanta. P_{bsb} and P_{rsb} are the transition probabilities to make a blue/red sideband to the $|1\rangle$ state and are given by

$$P_{rsb}(|1\rangle) = \sum_{n=0}^{\infty} P_n \sin^2(\Omega_{n,n-1}t/2), \qquad (6)$$

$$P_{bsb}(|1\rangle) = \sum_{n=0}^{\infty} P_n \sin^2(\Omega_{n,n+1}t/2)$$

$$= \sum_{n=0}^{\infty} P_{n+1} \sin^2(\Omega_{n,n-1}t/2). \qquad (7)$$

In the above equations the occupation probability for a thermal state distribution is $P(n) = (\frac{1}{1+\bar{n}})(\frac{\bar{n}}{1+\bar{n}})^n e^{-n\hbar\omega_x/k_BT}$, k_B is Boltzmann's constant, and $\Omega_{n,n+1}$ ($\Omega_{n,n-1}$) are the Rabi frequencies for the blue (red) sidebands.
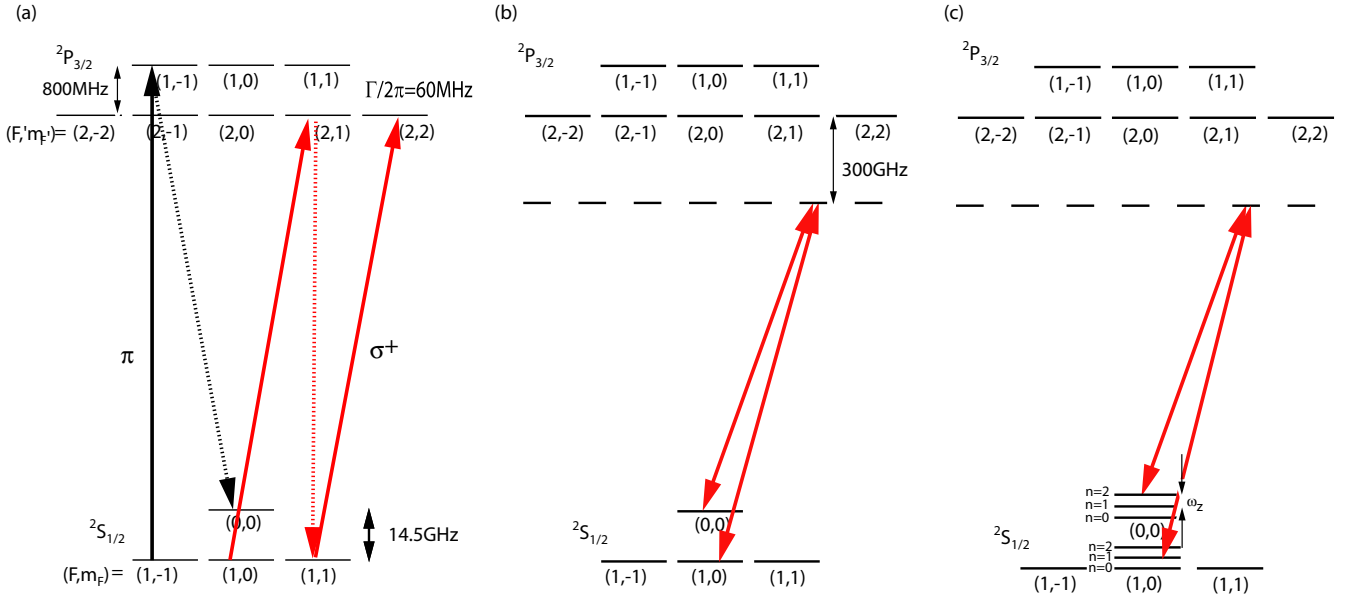
Figure 4. Energy level diagrams for ^{111}Cd$^+$ illustrating various qubit operations. (*a*) The dark arrow pointing from the $|F = 1\rangle$ manifold to the $|F' = 1\rangle$ manifold illustrates the initialization step. Applying π-polarized light tuned to the $|F = 1\rangle \rightarrow |F' = 1\rangle$ transition optically pumps any population in the $|F = 1\rangle$ states to the $|0\rangle$ qubit state. The light gray arrows depict the detection scheme. Applying σ^+ light resonant with the $|F = 1\rangle \rightarrow |F' = 2\rangle$ transition optically pumps any population occupying the $|1\rangle$ state to the $|F = 1, m_F = 1\rangle$ state. From here the population undergoes a cycling transition between $|F = 1, m_F = 1\rangle \rightarrow |F' = 2, m_{F'} = 2\rangle$. (*b*) Energy level diagram showing levels involved in stimulated Raman transitions. Two laser beams detuned from the excited state and with a frequency difference of $\omega_{HF}/2\pi = 14.53$ GHz drive the stimulated Raman transitions. These transitions can create any arbitrary superposition of the qubit states. (*c*) Energy level diagram for a motional stimulated Raman transition. Here the laser beams are detuned by $\omega_{HF} \pm \omega_z$, where ω_z is the trap frequency. These transitions allow access to the collective motional modes of the ion crystals.
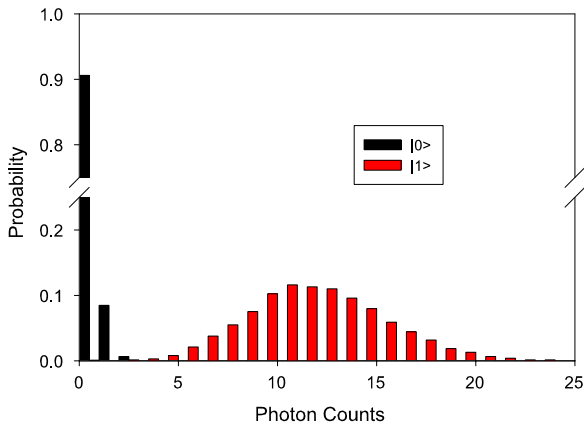

Figure 5. Detection histograms for a single ^{111}Cd$^+$ ion. For the data shown, each qubit state was independently prepared and measured with a PMT. Through the use of a discriminator that is set to distinguish the two distributions for counts greater than 1 or 2, a detection fidelity of 99.7% is achievable. Figure from [38].

Figure 6. Detection histograms for two ions. For this data set all four possible states were prepared. Detecting two ions is more complicated than a single ion since there can be a great deal of overlap between the double bright ion distribution and the single bright ion distribution. To prevent this, the count rate from double bright state is set high enough to minimize the overlap between the two outcomes. For two ions the highest detection fidelity possible using a PMT is 97%.

The first step in the cooling process is to Doppler cool the ions, this is achieved with the same light used for detection but now slightly detuned from resonance. After Doppler cooling the average vibrational mode of the motional population is $\bar{n} \sim 6$ (for a trap frequency of $\omega_z/2\pi = 5.8$ MHz) in ^{111}Cd$^+$. However, in order to implement coherent qubit operations, the ions must be localized to near the ground state and, therefore, a second cooling step is necessary. Raman sideband cooling techniques further cool the ions [39]. This is done by applying a sequence of pulses consisting of a blue sideband,
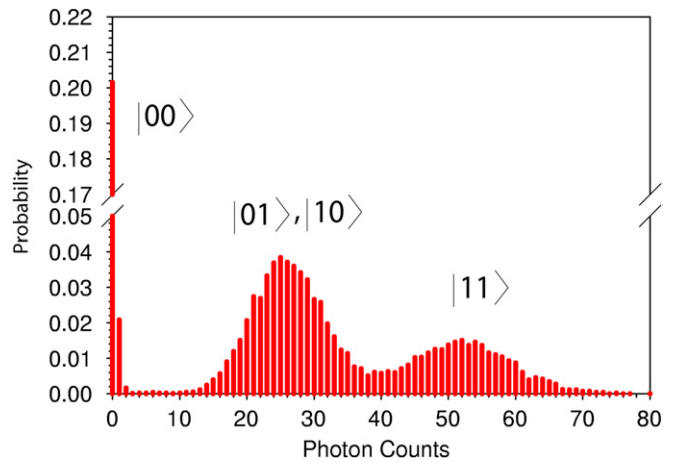
to lower the population by $\Delta\bar{n} = 1$ quanta on average, followed by a recycling pulse consisting of a spontaneous Raman transition. The spontaneous Raman transition does not appreciably change the vibrational level of the ions on average in the LDL, but only re-initializes the system. This pulse sequence is repeated many times and when the ion reaches the ground state, further cooling pulses have no effect since
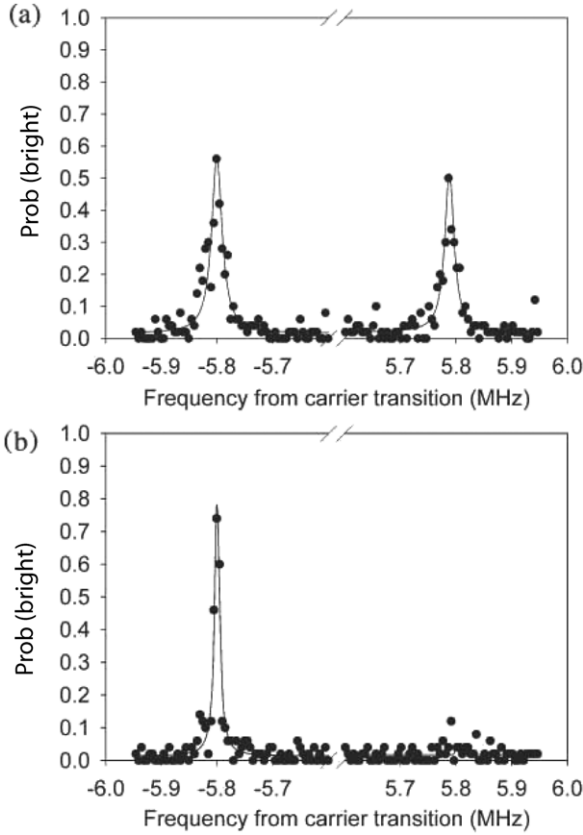
Figure 7. Plot illustrating sideband spectrum of a (*a*) Doppler cooled and (*b*) Raman sideband cooled ion. The plots show the probability to be in the bright state versus detuning from carrier transition for a trap frequency of $\omega_z = 2\pi \times 5.8$ MHz. (*a*) After Doppler cooling $\bar{n} \sim 6$. (*b*) After Raman sideband cooling $\bar{n} \sim 0.05$. The hallmark of a cooled ion is a disappearance of the blue sideband, as can be seen in the lower plot. Figure from [40].

the blue sideband transition is no longer possible. A sideband spectrum showing a Doppler cooled ion ($\bar{n} \sim 6$) and a Raman sideband cooled ion ($\bar{n} \sim 0.05$) is shown in figure 7 [40]. Note that for the sideband cooled case the blue sideband is nearly zero.

Sympathetic cooling is another possible cooling scheme. In this scheme, a second refrigerator ion is cooled and then sympathetically cools the qubit ion through the Coloumb interaction. For this process one either needs a different isotope of the qubit atomic species or a different atomic species. This is so that the cooling light for the refrigerator ion does not interfere with the information stored in the qubit states. Figure 8(*a*) shows a $^{112}\text{Cd}^+$ ion Doppler cooled by a $^{114}\text{Cd}^+$ ion [41]. Note that the light to cool the $^{114}\text{Cd}^+$ ion has a minimal effect on the neighboring $^{112}\text{Cd}^+$ ion. Other sympathetic cooling experiments have been carried out including one with two different atomic species, $^9\text{Be}^+$ and $^{24}\text{Mg}^+$ ions [42], and one with a pair of $^{40}\text{Ca}^+$ ions [43], only in these cases the ions were sympathetically ground state cooled. This scheme may be especially useful for larger ion trap arrays that will require shuttling the ions from zone to zone [44]. Refrigerator ions will have to be kept in the different zones to recool the qubits after transport [45–47].
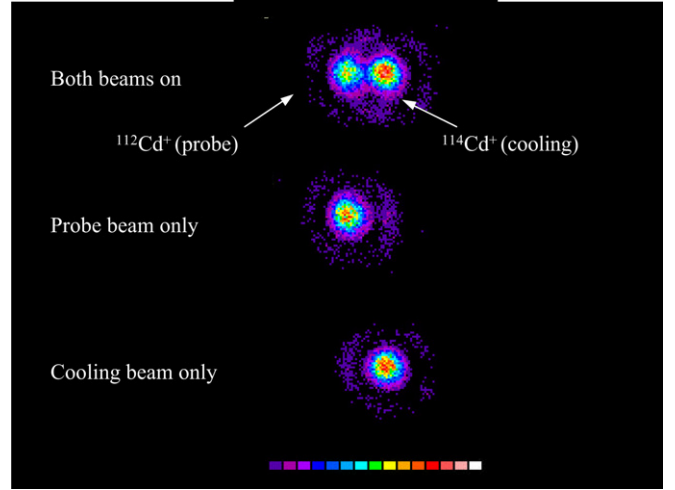

Figure 8. Two different isotopes of Cd, $^{112}\text{Cd}^+$ ion with a $^{114}\text{Cd}^+$, are confined in an asymmetric quadrupole trap. In the top picture the $^{114}\text{Cd}^+$ is being cooled while a probe beam is illuminating the $^{112}\text{Cd}^+$ ion. The middle picture shows only the $^{112}\text{Cd}^+$ ion with the probe beam on and the lower picture shows the $^{114}\text{Cd}^+$ ion with just the cooling beam applied. Figure from [41].

3.5. Single qubit gates

The trapped ion system can be thought of as a harmonically bound spin-1/2 magnetic moment in a constant magnetic field [48]. This two-level system is a valid approximation since the applied light strongly couples the two qubit levels and only weakly couples to off-resonant states. We can write the Hamiltonian as

$$H_0 = \frac{\hbar\omega_{\text{HF}}}{2}\hat{\sigma}_z + \hbar\omega_z \hat{a}^\dagger \hat{a}. \qquad (8)$$

Here $\hat{\sigma}_z = \begin{bmatrix} 1 & 0 \\ 0 & -1 \end{bmatrix}$ is the Pauli spin operator matrix, $\hbar\omega_{\text{HF}}$ is the natural energy splitting between the two qubit states, $\hat{a}$ and $\hat{a}^\dagger$ are the raising and lowering (creation and annihilation) operators and ω_z is the frequency of motion along the z-axis (we assume that the other modes of motion are sufficiently spectrally resolved and are not altered).

When an external electromagnetic field is applied, the Hamiltonian becomes $H_T = H_0 + H'$, where the perturbation Hamiltonian is $H' = -\mu_b \cdot B(r, t)$. Here μ_b is the effective magnetic dipole moment of the two-level system, $B(r, t)$ is the applied effective magnetic field.

Experimentally the coupling mechanism does not need to be a real magnetic dipole interaction, but it will yield a Hamiltonian of the form

$$H' = \frac{\hbar\Omega}{2}(\sigma_+ e^{i(kr-\omega t+\phi)} + \sigma_- e^{-i(kr-\omega t+\phi)}), \qquad (9)$$

where $\Omega = -\mu_b B_x/2\hbar$ is the Rabi frequency, $\sigma_+ = \begin{bmatrix} 0 & 1 \\ 0 & 0 \end{bmatrix}$ and $\sigma_- = \begin{bmatrix} 0 & 0 \\ 1 & 0 \end{bmatrix}$.

For now, we will assume a scenario where the magnetic field propagates such that $k \cdot z = 0$, that is the magnetic field propagation is perpendicular to the direction of the harmonic potential. Since the photons have no momentum in the z-direction, they cannot couple to the harmonic oscillator levels

in this interaction. Later in the section we will discuss the more general case when $k \cdot z \neq 0$, but for the present case it is not necessary. Under this assumption the factor $e^{ik \cdot r}$ will contribute at most a phase factor of e^{ikr_0}, which can be absorbed into the phase ϕ.

Transforming equation (8) into the interaction picture and applying the rotating wave approximation (RWA) gives

$$H_{\mathrm{I}} = \frac{\hbar\Omega}{2}(\sigma_+ e^{-i(\delta\omega t + \phi)} + \sigma_- e^{i(\delta\omega t + \phi)}). \tag{10}$$

Here $\delta\omega = \omega - \omega_0$ is the field detuning from resonance. The solution to the Rabi two-level problem is [49]

$$\dot{c}_{\uparrow,n} = \frac{i\Omega}{2}e^{-i((\delta\omega)t+\phi)}c_{\downarrow,n},$$

$$\dot{c}_{\downarrow,n} = \frac{-\Omega}{2}e^{i((\delta\omega)t+\phi)}c_{\uparrow,n}, \tag{11}$$

where $c_{m,n}(t)$ are the amplitudes of the corresponding levels $|m\rangle|n\rangle$ for the qubit state in the rotating frame $|\Psi(t)\rangle = \sum_{n=1}^{\infty}(c_{\uparrow,n}(t)e^{-i\omega_0 t/2}|\uparrow\rangle + c_{\downarrow,n}(t)e^{i\omega_0 t/2}|\downarrow\rangle)e^{in\omega_z t}|n\rangle$. When $\delta\omega = 0$ the field is on resonance and the state evolves under the time-evolution operator $U(t)$ by $|\Psi(t)\rangle = \hat{U}(t)|\Psi(0)\rangle$, here $\hat{U}(t)$ is defined as (in the $c_{\uparrow,n}$, $c_{\downarrow,n}$ basis),

$$\hat{U}(t) = \begin{bmatrix} \cos\left(\dfrac{\Omega t}{2}\right) & -ie^{-i\phi}\sin\left(\dfrac{\Omega t}{2}\right) \\ ie^{i\phi}\sin\left(\dfrac{\Omega t}{2}\right) & \cos\left(\dfrac{\Omega t}{2}\right) \end{bmatrix} = R(\Omega t, \phi).$$

$$\tag{12}$$

$R(\Omega t, \phi)$, is a rotation on the Bloch sphere by $\theta = \Omega t$. We define the following rotations using equation (12): $R_x(\theta) = R(\theta, 0)$ is a rotation about the x-axis and $R_y(\theta) = R(\theta, \pi/2)$ is a rotation about the y-axis. For a universal quantum computer we need to be able to make rotations in all three directions, x, y and z, but equation (12) only allows us to make rotations in x and y. To make a z-rotation we use a composite pulse sequence consisting of x and y rotations through the following: $R_z(\theta) = R_x(\pi/2)R_y(\theta)R_x(-\pi/2)$. This is equivalent to applying a phase shift of θ to the ions. Since we have control over both Ωt and ϕ, equation (12) allows us to make rotations giving any superposition of $\alpha|0\rangle + \beta|1\rangle$, therefore fulfilling the requirement for the single qubit rotations.

In practice, the single qubit rotations are achieved with either resonant microwaves or with optical Raman transitions. Optical Raman transitions can be used for single qubit operations but also allow access to the motional sidebands needed for entangling operations.

A Raman transition is a stimulated two photon transition involving three levels, here the levels are the two qubit states $|0\rangle$ and $|1\rangle$ and the excited $^2P_{3/2}$ state, $|e\rangle$. Two laser beams detuned from the excited state by Δ and with frequency splitting equal to the frequency difference between the two qubit levels, $\omega_{\mathrm{HF}}/2\pi = 14.5$ GHz for ^{111}Cd$^+$, can drive transitions between the spin states, as shown in figure 4. We represent the field from each laser beam by $E_q(r) = \hat{E}_q(r)\cos(k_q \cdot r - \omega_q t - \phi_q)\epsilon_q$, where $q = a, b$ are the two different electric fields. Following the same formalism
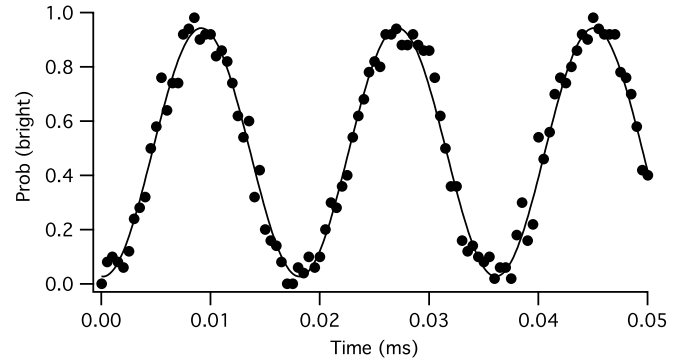

Figure 9. Stimulated Raman–Rabi flopping on the carrier transition $|0, n = 0\rangle \rightarrow |1, n = 0\rangle$ for a detuning of $\Delta = 2\pi \times 150$ GHz, with $\Omega = 2\pi \times 55$ kHz. The ion is initialized to the $|0\rangle$ state and within ~ 0.01 ms the population is transferred to the $|1\rangle$ state. This time is often referred to as the π-pulse time. Stopping halfway in between results in the superposition state $(|0\rangle + |1\rangle)/\sqrt{2}$, and this is often called a $\pi/2$ pulse.

as above but now replacing $\mu_b \cdot B(r, t)$ with $\mu_d \cdot (E_a(r, t) + E_b(r, t))$ using the above electric fields, assuming $k \cdot z \neq 0$ (to access the motional levels), and accounting for the Stark shift from the laser beams, equation (10) becomes [50]

$$\hat{H}_{\mathrm{I}} = \frac{\hbar\Omega}{2}(\hat{\sigma}_+ e^{i\eta(\hat{a}e^{-i\omega t} + \hat{a}^\dagger e^{i\omega t})}e^{-i(\delta\omega')t}e^{i(\Delta kr_0 + \Delta\phi)} + \text{h.c.}). \tag{13}$$

Here μ_d is the electric dipole operator, $\Omega = g_1 g_2/2\Delta$, $g_{1,2}$ are the coupling strengths between the ground and excited state, $\delta\omega' = \omega_b - \omega_a - \omega_0'$ is the detuning from the Stark shifted resonance, $\omega_0' = \omega_0 + \chi_-$ when the fields a and b are turned on, $\chi_- = (\chi_{|0\rangle} + \chi_{|1\rangle})/2$ is the difference in the Stark shift between the qubit states and Δk is the difference in wavevectors between the two fields.

With these beams we can either drive a pure spin flip transition as shown in figure 9 or we can access the motional modes $|n\rangle$ and drive transitions such as $|\uparrow\rangle|n\rangle \rightarrow |\downarrow\rangle|n'\rangle$, we do this by controlling the frequency splitting between the applied beams. A beatnote of $\omega_{\mathrm{HF}}/2\pi = 14.53$ GHz (in ^{111}Cd$^+$) allows us to transfer population between the two qubit states and a beatnote of $\omega_{\mathrm{HF}} \pm \omega_z$ allows us access to the motional modes, where ω_z is the trap frequency. Figure 4(c) depicts the laser beam frequencies needed to drive the motional transitions.

One source of decoherence during the stimulated Raman transitions is spontaneous emission from off-resonant coupling while the laser beams are turned on. The amount of spontaneous emission depends on both the intensity of the light and the amount of detuning from the excited state. The best way to understand how spontaneous emission effects the experiments is to compare the spontaneous emission rate for large detunings, $\gamma_p = s\gamma^3/(4\Delta^2)$, to the Raman transition rate, $\Omega = s\gamma^2/\Delta$, where γ is the excited state linewidth, I_{sat} is the saturation intensity, $s = I/I_{\mathrm{sat}}$ is the saturation parameter and Δ is the laser detuning from the excited state. This gives $\gamma_p/\Omega = \gamma/(2\Delta)$ which means that in the time it takes the ion to undergo a complete spin flip, the qubit has a $\gamma/(2\Delta)$ chance of undergoing a spontaneous emission event and therefore decaying to the ground state incoherently. As can be seen from the above equation, the spontaneous emission rate
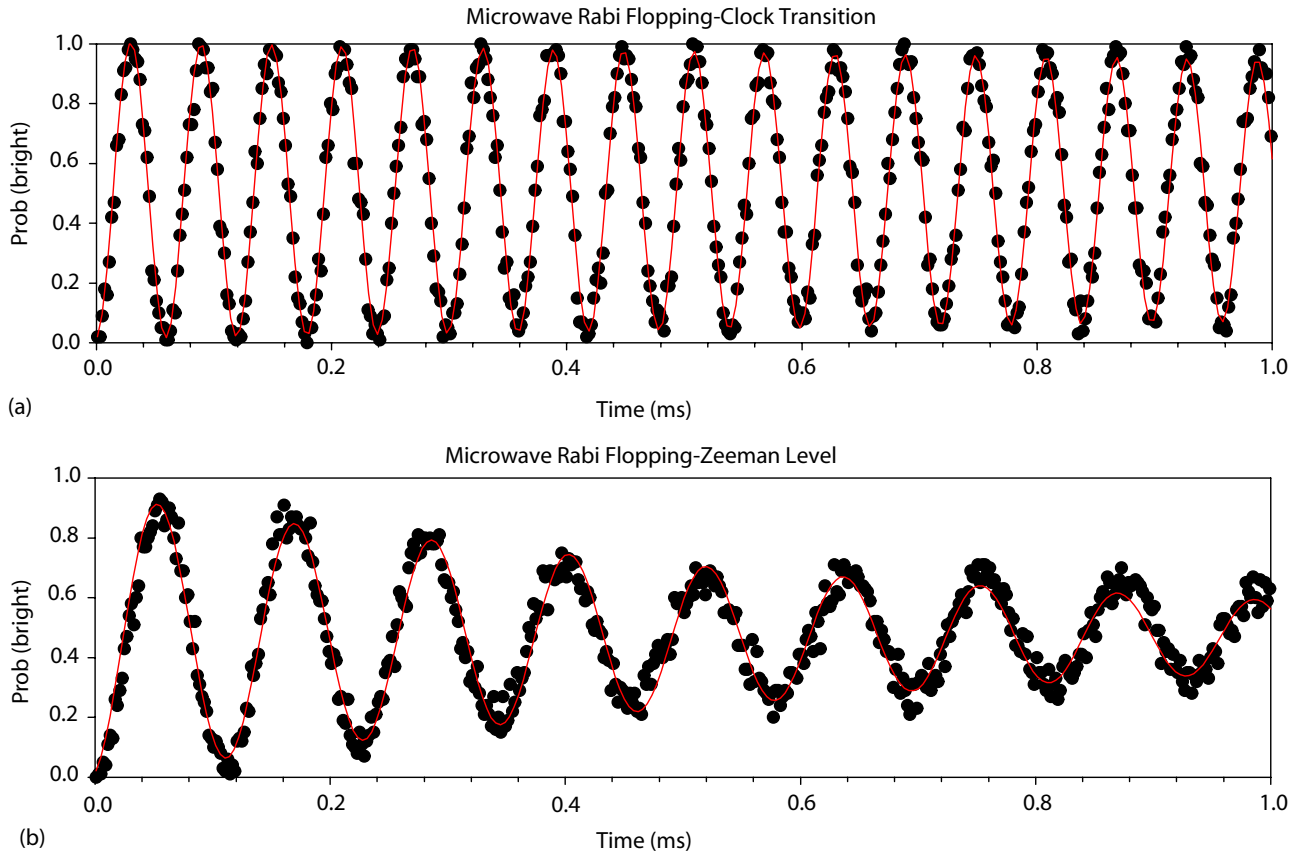
Figure 10. Microwave Rabi flopping on the carrier $|0\rangle \rightarrow |1\rangle$ transitions and $|0\rangle \rightarrow |F = 1, m_{F=1}\rangle$ Zeeman transition. Both plots were taken with 1 W of power applied to a microwave horn. The carrier transition oscillates at about twice the frequency of the Zeeman level due to polarization of the microwaves. The Zeeman levels are clearly more sensitive to magnetic field fluctuations than the carrier.

scales as $1/\Delta$ and so the larger the detuning, the smaller the spontaneous emission rate. But this condition only holds if the detuning is much less than the fine structure splitting and coupling to other excited states is negligible [51].

Microwaves can also be used to drive single qubit rotations. Figure 10 shows microwave Rabi flopping for both the clock state qubits, $|0\rangle \rightarrow |1\rangle$, and the Zeeman transition, $|\uparrow\rangle \rightarrow |F = 1, m_F = 1\rangle$. In the lower plot a magnetic field is applied to the ion to split the Zeeman levels. This plot clearly shows how sensitive the Zeeman levels are to magnetic field fluctuations compared with the clock state qubits in $^{111}Cd^+$. This is not surprising since the sensitivity of the clock states to magnetic field noise in $^{111}Cd^+$ is $\delta\nu_{clock} = (600 \, Hz \, G^{-2}) B\delta B$ whereas the Zeeman levels sensitivity is $\delta\nu_{clock} = (1.4 \, MHz \, G^{-1})\delta B$. At a magnetic field of 3.25 G, the Zeeman levels are about 620 times more sensitive to magnetic field fluctuations than the clock states.

3.6. Phonon-mediated entangling gates

The most critical component of trapped ion quantum computing is the entangling operations. By coupling to the collective motional states (phonon modes) of the ion crystal, entangling operations can be implemented between any two ions in the linear crystal and are not limited to nearest neighbor pairs. This section will describe the theory of the three main trapped ion entangling gates that have been used. The

experimental implementations and applications of each will follow in the next section.

The first trapped ion entangling gate was proposed in 1995 by Cirac and Zoller [11]. They suggested to entangle the spins states of the ions by coupling to the collective motional mode. The steps of the gate are as follows.

 (i) Cool the ion crystal to its motional $n = 0$ ground state.
 (ii) Apply a laser beam to ion j to map the spin state of j onto the collective motional state of the ion string. A motional state will only be excited if ion j is in a particular spin state, $|1\rangle$ for example.
(iii) Apply a second laser beam sometime later to ion k. If a motional mode is present then this laser pulse will flip the spin of ion k, otherwise ion k will remain unaffected.
(iv) Reverse step one to map the motional state back onto the spin state for measurement.

The outcome of this gate is to take the superposition state $(|0\rangle + |1\rangle)_j|0\rangle_k$ to the entangled state $|0\rangle_j|0\rangle_k + |1\rangle_j|1\rangle_k$. This gate can be difficult to implement due to the tight restrictions of the ions needing to be cooled to the absolute ground state of motion and having to tightly focus laser beams to address only one ion in the linear crystal. Typically, the ions are only separated by a few micrometers. Shortly after the Cirac and Zoller proposal, other theoretical proposals were suggested that relied on using spin dependent forces to entangle the ions. These proposals by Milburn [52] and Mølmer and Sørensen
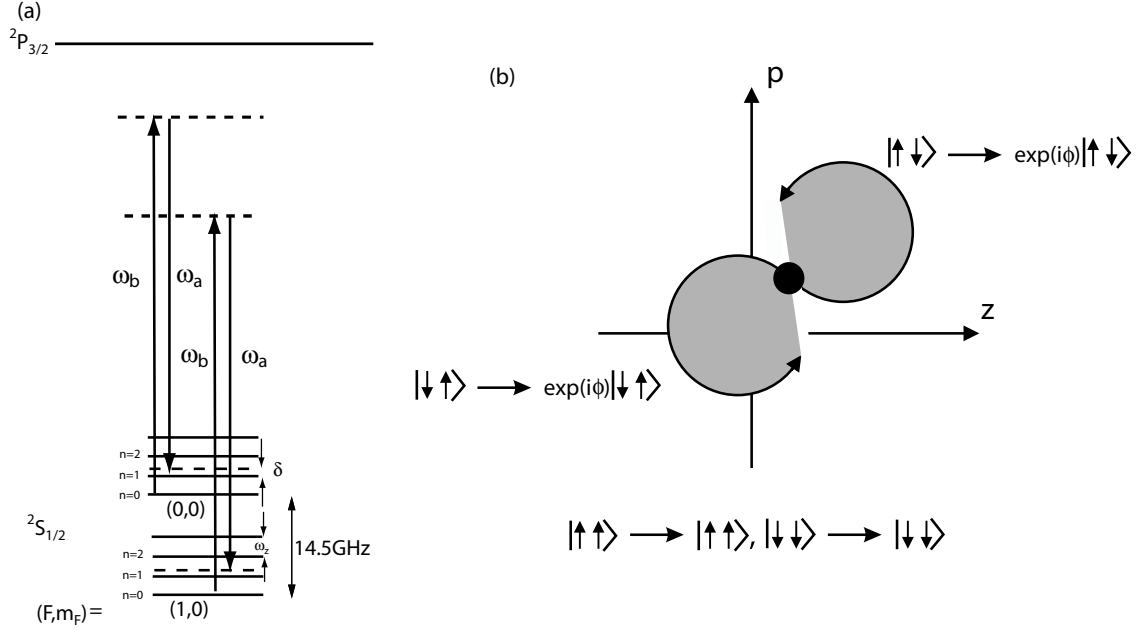
Figure 11. Energy level and phase space diagram for the σ_z gate. (*a*) Energy level diagram illustrating beam configuration for the σ_z gate. Two laser beams with a frequency splitting of $\omega_b - \omega_a = \omega_z + \delta$ generate the necessary coupling for the gate. (*b*) Phase space evolution of states when σ_z gate is applied [54]. The gate causes the states $|01\rangle$ and $|10\rangle$ to evolve in phase space while the $|00\rangle$ and $|11\rangle$ states remain stationary. Phase space diagram from [54]. Reprinted with permission from MacMillan Publishers Ltd, copyright (2003).

(M–S), [53] relax the stringent requirements on ground state cooling and individual addressing. Both of these gates rely on creating a spin dependent force on the ions that results in a geometric phase being accumulated by a particular state.

Applying a classical force of the form $f(t) = F \sin[(\omega - \delta)t + \phi]$ to a harmonic oscillator leads to a displacement operator $D(\alpha)$ that will translate the motional states in position/momentum space and results in coherent states of the form $|\alpha\rangle = e^{-1/2|\alpha|} \sum_{n=0}^{\infty} \frac{\alpha^n}{\sqrt{n!}} |n\rangle$ [50]. Applying two sequential displacements gives $D(\alpha)D(\beta) = D(\alpha + \beta)e^{i \text{Im}(\alpha\beta^*)}$, where the imaginary component, $\text{Im}(\alpha\beta^*)$, is the geometric phase accumulated during the operation. The time-evolution operator is $U(t) = e^{i\Phi(t)} D(\alpha(t))$ and the geometric phase accumulated over the path from time 0 to t is $\Phi(t) = \text{Im}[\int_0^t \alpha(t') \, d\alpha(t')]$. In the rotating frame of motion and for a near resonant driving force detuned by δ, the initial motional state moves in a circular trajectory with radius $F/(2\hbar\delta)$ and period $T = 2\pi/\delta$. The path the state follows is $\alpha(t) = F z_0/(2\hbar\delta)(1 - e^{i\delta t})$ and, in one revolution, the motional state returns to the starting position. Under this evolution the state acquires a geometric phase equal to the area enclosed by the trajectory, which is $\Phi_0 = \pi |F z_0|^2 / 2\hbar^2\delta^2$.

Applying a spin dependent force to a single ion gives the Hamiltonian [50]

$$H_I = \sum_{m=|0_n\rangle, |1_n\rangle} \left(\frac{F_m^* z_0}{2} \hat{a} e^{-i\delta t} + \frac{F_m z_0}{2} \hat{a}^\dagger e^{i\delta t} \right) |m\rangle\langle m|, \quad (14)$$

where m is the internal qubit state of the ion and $|0_n\rangle$ and $|1_n\rangle$ are the eigenstates of $\hat{\sigma} \cdot \boldsymbol{n}$ with eigenvalues $+1$ and -1, respectively. Writing this Hamiltonian in terms of the $\sigma \cdot \boldsymbol{n}$

operator gives

$$H_I = \left(\frac{F_+^* z_0}{2} \hat{a} e^{-i\delta t} + \frac{F_+ z_0}{2} \hat{a}^\dagger e^{i\delta t} \right) \hat{I}$$
$$+ \left(\frac{F_-^* z_0}{2} \hat{a} e^{-i\delta t} + \frac{F_- z_0}{2} \hat{a}^\dagger e^{i\delta t} \right) \hat{\sigma} \cdot \boldsymbol{n}. \quad (15)$$

Here $\hat{I}$ is the identity operator and $F_\pm = (F_{|0\rangle_n} \pm F_{|1\rangle_n})/2$. The first term of equation (15) has no effect on the dynamics of the system and so can be ignored. Under this Hamiltonian the wavefunction evolves in time as

$$|\Psi(t)\rangle = \sum_{m=\uparrow_n, \downarrow_n} a_m e^{i\Phi(t)} |m\rangle |\alpha_m(t)\rangle, \quad (16)$$

where a_m is the initial amplitude of the state $|m\rangle$, $\alpha_m(t) = (F_m z_0/2\hbar\delta)(1 - e^{i\delta t})$ is the coherent state of spin $|m\rangle$ and $\Phi(t)$ is the geometric phase.

Making the last term of equation (15) proportional to $\sigma \cdot z$ creates a differential force on the eigenstates of the unperturbed Hamiltonian [52]. This σ_z interaction does not require direct coupling between the two qubit spin states, but instead involves coupling between the different vibrational levels of the same spin state, as shown in figure 11. A convenient feature of this gate is that it does not require the Raman beams to bridge the hyperfine splitting between the qubit states, but only the smaller vibrational spacing. This gate relies on a differential ac Stark shift to provide a spin dependent force on the two spin states of the ion. When the beams are applied, the ion essentially sees a moving periodic potential that exerts a force on the ions in the direction of the laser beam travel. The ions will feel a force proportional to the ac Stark shift amplitude, and so, if the ac Stark shift has a different amplitude for each spin state, then the two spin states experience different forces [54].
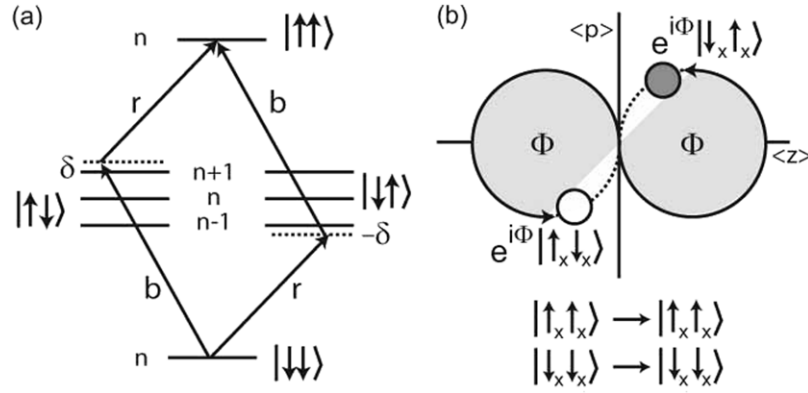
Figure 12. Two views of the Mølmer–Sørensen σ_x entangling gate for two ions in (a) energy space [53] and (b) motional phase space [54] for the gate-diagonal spin basis. The quantum number n and phase space coordinates describe a given collective motional mode. Red and blue Raman sideband couplings are labeled by r and b and have detuning $\delta_r = \delta = -\delta_b$. Unlike the original gate proposal, the variation shown here relies on near resonant detunings to the vibrational levels. In phase space this results in larger diameter trajectories and allows a $\pi/2$ phase shift after one complete evolution. Figure from [56].

This σ_z force only works if a differential ac Stark shift exists between the two qubit levels, which is not always the case. The magnetic field insensitive clock state transitions have no differential ac Stark shift when $\Delta \gg \omega_0$ and so this gate scheme is not plausible for these levels [50]. Instead we must use magnetic field sensitive transitions as the qubit levels for this gate.

Applying this force to two ions in the stretch mode of motion for a phase that corresponds to one full evolution in phase space results in the following wavefunction evolution

$$
\begin{aligned}
|00\rangle|\Psi\rangle &\rightarrow |00\rangle|\Psi\rangle, \\
|01\rangle|\Psi\rangle &\rightarrow e^{i\pi/2}|01\rangle|\Psi\rangle, \\
|10\rangle|\Psi\rangle &\rightarrow e^{i\pi/2}|10\rangle|\Psi\rangle, \\
|11\rangle|\Psi\rangle &\rightarrow |11\rangle|\Psi\rangle = e^{-i\pi}(e^{i\pi/2}|1\rangle)(e^{i\pi/2}|1\rangle).
\end{aligned}
\tag{17}
$$

This is equivalent to a π-phase gate with additional $\pi/2$-phases on the $|1\rangle$ states. During an algorithm these additional $\pi/2$-phases can be absorbed into the surrounding single qubit rotations for the corresponding qubit [54].

If instead we make the last term of equation (15) proportional $\sigma \cdot \phi$, we create a gate that does rely on direct coupling between the qubit spin states [55]. Here $\hat{\sigma}_\phi = e^{-i\phi_s}\hat{\sigma}_+ + e^{i\phi_s}\hat{\sigma}_-$, where the azimuthal angle ϕ_s defines the orientation of the force's spin and $\hat{\sigma}_\pm$ are the spin raising and lowering operators. When $\phi_s = 0$ the gate is reduced to a σ_x coupling [55]. Since this gate does not rely on a differential Stark shift between the two involved states, it can be applied to the magnetic field insensitive clock states. As a result this gate is less sensitive to decoherence compared with the σ_z gate.

Figure 12 shows two different views of the Mølmer–Sørensen entangling gate on two ions. Part (a) is the energy level diagram for near resonantly detuned red and blue sideband pulses. The phase space trajectory is shown in part (b). For closed trajectories in phase space, the geometric phase Φ depends on the area enclosed [55].

This spin dependent displacement entangles the spin and motion, but when the trajectory of the states is closed, the spin and motion become disentangled and a spin dependent geometric phase $\Phi = 2\pi m(\eta\Omega/\delta)^2$ is applied to the gate basis. A maximally entangled state occurs when a geometric phase of $\pi/2$ is applied. This is implemented in the fastest possible time with $m = 1$ and necessitates that $\delta = 2\eta\Omega$ and the gate time is set to $\tau = 2\pi/\delta$. Written in the σ_z basis the gate truth table is

$$
\begin{aligned}
|00\rangle &\rightarrow \Psi_1 = \frac{1}{\sqrt{2}}|00\rangle + ie^{i\phi_{s1}+\phi_{s2}}|11\rangle, \\
|11\rangle &\rightarrow \Psi_2 = \frac{1}{\sqrt{2}}|11\rangle + ie^{i\phi_{s1}+\phi_{s2}}|00\rangle, \\
|01\rangle &\rightarrow \Psi_3 = \frac{1}{\sqrt{2}}|01\rangle + ie^{i\phi_0}|10\rangle, \\
|10\rangle &\rightarrow \Psi_4 = \frac{1}{\sqrt{2}}|10\rangle + ie^{i\phi_0}|01\rangle.
\end{aligned}
\tag{18}
$$

The phases ϕ_0, ϕ_{s1} and ϕ_{s2} have been included in the even and odd parity states to account for the effect of both ac Stark shifts and Raman laser coherences [56]. When $\phi_0 = \phi_{s1} = \phi_{s2} = 0$, the gate is reduced to a σ_x coupling. The red and blue sideband driving fields must be well controlled as both the spin phase ϕ_{si} and motional phase ϕ_m depend critically on these driving fields ϕ_r and ϕ_b as $\phi_s = (\phi_b + \phi_r)/2$ and $\phi_m = (\phi_b - \phi_r)/2$ [56]. The motional phase does not appear in the above equations because the motional mode is only relevant during the gate pulse. The motional state returns to the ground state after the gate pulse is applied and becomes a global variable. Only the spin phase remains at the end of the gate.

3.7. Scaling issues

An important issue in ion trapping is decoherence due to unwanted heating of the ions. All of the ion trapping systems built thus far have been plagued by an anomalous heating rate that is orders of magnitude above the predictions for the heating

rate expected from Johnson noise [57, 58]. It is believed that this additional heating arises from noisy patch potentials on the electrodes that are being driven at rf frequencies close to the secular frequencies of the ions [58].

This heating will become a bigger problem as the ion traps scale down since it is predicted that the heating rate for fluctuating patch potentials scales as $1/d^4$ [57]. To study this problem an ion trap was constructed with the capability to cool down the trap electrodes [58]. In addition, the trap was fabricated with moving needle electrodes so that the distance from the ion to the electrode could be changed *in situ* from 30 to 250 μm [58]. The results from this experiment support the idea of noisy patch potentials and conclude that to reduce the anomalous heating the trap electrodes will have to be cooled down. Reducing the temperature of the electrodes by a factor of 2 decreased the heating rate by over one order of magnitude [58]. Similar results were seen in a $^{88}Sr^+$ surface ion trap where the electrodes were cooled down to 6 K and the heating rate dropped by 7 orders of magnitude [59].

As the trap designs become more complex, this heating will be an especially important issue. Some of the newer ion traps are fabricated using microelectromechanical systems (MEMS) technology with typical electrode distances on the order of 50 μm, due to the shallow depth of these traps it is necessary to control the anomalous heating, otherwise the ions will be lost during qubit operations [60, 61].

4. State of the art: algorithms and operations

Harnessing the power of entangled superpositions would allow certain quantum algorithms to be performed that are faster than classical algorithms. The most well-known quantum computing algorithm is Shor's factoring algorithm, which can factor large numbers exponentially faster than any known classical algorithm [7]. The realization of this algorithm would render many current encryption schemes obsolete, as these schemes rely on the inability of classical computers to efficiently factor large numbers. Two other popular quantum computing algorithms are the Deutsch–Jozsa algorithm that was described in the introduction [6] and Grover's quantum database search which allows polynomial speed up in the time it takes to search an unsorted database [62]. This section will cover the experimental realizations of the gates discussed in the previous section and detail the algorithms implemented with these entangling gates. A general overview of many of the algorithms will be given and a detailed description of Grover's algorithm with two qubits will be presented.

4.1. Phonon-mediated gates

In 2003 the Cirac–Zoller gate, described in the previous section, was implemented with two $^{40}Ca^+$ ions [63]. A previous demonstration was executed between the spin and motional states of a single trapped ion [12], but this is the first two-ion implementation. The $S_{1/2}$ ground state and the metastable $D_{5/2}$ state serve as the $|0\rangle$ and $|1\rangle$ qubit states, respectively. The ions were confined in a linear rf-Paul trap and were cooled to the $|n = 0\rangle$ ground state of motion with 99%
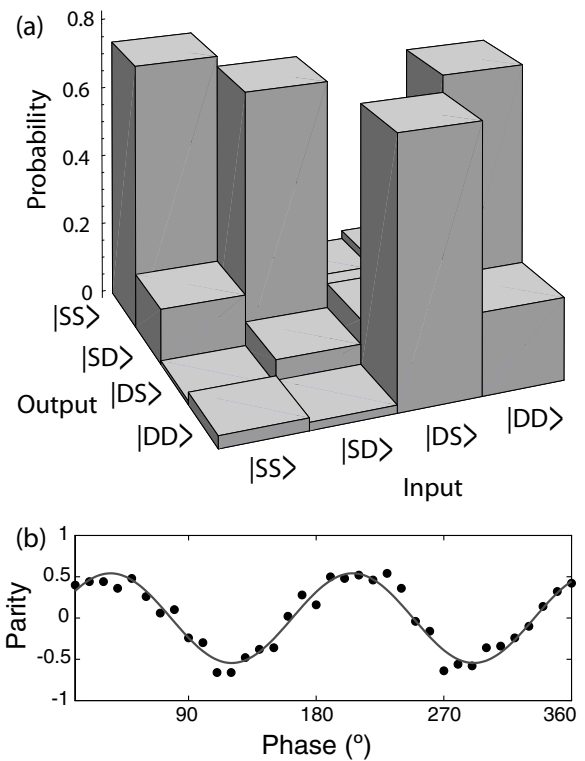

Figure 13. Cirac–Zoller CNOT gate operation. (*a*) Experimentally observed truth table of the Cirac–Zoller CNOT operation derived from joint-probability measurements as in figure 2. Ideally, the table should reproduce the squared moduli of the entries of the unitary operation. Experimentally, it is found that the currently available fidelity of the gate operation is limited to about 70–80%. (*b*) Cirac–Zoller gate operation with a superposition $1/\sqrt{2}(|S\rangle + |D\rangle)|S\rangle$ as input results in an entangled output state $1/\sqrt{2}(|SS\rangle + e^{i\alpha}|DD\rangle)$. The entanglement is analyzed by applying $\pi/2$-pulses with phase ϕ to both ions after the gate operation and by measuring the parity as a function of the phase ϕ. The quantum nature of the gate operation is proved by observing oscillations with $\cos(2\phi)$, whereas a non-entangled state would yield a variation with $\cos(\phi)$ only. From the observed visibility of 0.54(3) and the observed populations $P_{SS} = 0.42(3)$ and $P_{DD} = 0.45(3)$ prior to the analyzing pulses a fidelity of $F = 0.71(3)$ is calculated. Figure from [63]. Reprinted with permission from MacMillan Publishers Ltd, copyright (2003).

fidelity via sympathetic sideband cooling techniques [43]. The breathing (stretch) mode of motion $\omega_b = 2\pi \times 2.1$ MHz was used as the databus and the ion-qubit states were initialized by optical pumping. The experimental truth table of the gate is shown in figure 13, a fidelity of 70–80% was achieved. The main decoherence source was due to laser-frequency noise which limits the phase coherence between the qubits. Other decoherence sources include addressing errors when tightly focusing on the target ion and off-resonant excitations during the application of the blue sideband pulses [63].

As stated earlier, the Cirac–Zoller gate can be difficult to implement due to the tight restrictions on cooling to the $|n = 0\rangle$ ground state of motion and addressing single ions with tightly focused laser beams. As a result, many experimental groups have switched to gates that rely on spin dependent forces to entangle the ions. These gates are commonly called geometric phase gates and considerably relax the requirements on ground
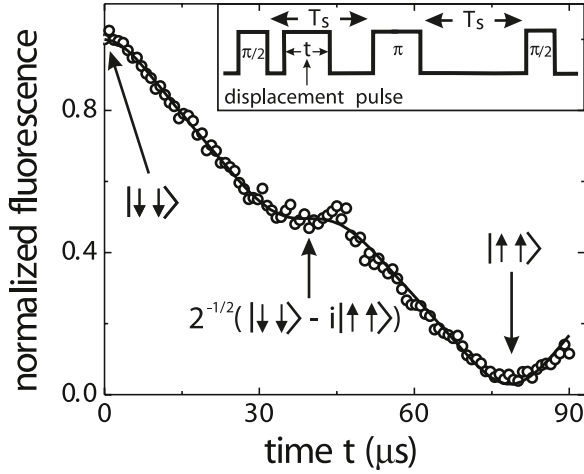
Figure 14. State evolution upon displacement. Normalized fluorescence signal after inserting a displacement pulse of variable duration into a spin-echo experiment that is applied to the $|\downarrow\downarrow\rangle|0\rangle$ state (see inset). The motional state returns to its point of origin after 39 μs, leading to an approximate state $2^{-1/2}(|\downarrow\downarrow\rangle - i|\uparrow\uparrow\rangle)|0\rangle$ after 39 μs and to the approximate state $|\uparrow\uparrow\rangle|0\rangle$ after 78 μs. The solid line is a fit to the theoretically expected signal that also allows for an exponential decay in contrast with detuning and decay constant as free parameters. After 39 μs, the fitted decay constant $\tau_0 = 1.3$ ms predicts a contrast of 0.97, in good agreement with the independently determined fidelity of the entangled state for this gate time. Figure from [54]. Reprinted with permission from MacMillan Publishers Ltd, copyright (2003).

state cooling and do not require tightly focused laser beams to individually address the ions.

The σ_z gate was experimentally demonstrated with two ^{9}Be$^+$ ions confined in a linear trap on the stretch mode of motion, $\omega_s = 2\pi \times 6.1$ MHz [54]. The ground state hyperfine levels $|F = 2, m_F = -2\rangle \equiv |\downarrow\rangle$ and $|F = 1, m_F = -1\rangle \equiv |\uparrow\rangle$ serve as qubit states. Both ions were ground state cooled with Raman sideband cooling and the qubit states were initialized through optical pumping. The state-dependent displacement force resulting in a Hamiltonian of the form of equation (14) results from Raman laser beams detuned by $\Delta\omega = \omega_s - \delta$, close to the frequency of the stretch mode of motion ω_s, where $|\omega_s| \gg |\delta|$. Application of these laser pulses results in ion evolution given by equation (17). The experimental results are detailed in figure 14, the entangled states were created with 97% fidelity. Figure 15 illustrates parity versus phase of an analysis $\pi/2$ pulse scan applied to the state after the gate pulses. The parity $\Pi = (P_{\uparrow\uparrow} + P_{\downarrow\downarrow}) - (P_{\uparrow\downarrow} + P_{\downarrow\uparrow})$ gives direct information about the off-diagonal elements of the density matrix, and so, when combined with the fluorescence measurements can be used to estimate the fidelity. The main decoherence sources here are fluctuations in δ, Raman laser beam intensity fluctuations, and spontaneous emission events during the Raman beam application [54].

The σ_x gate was experimentally implemented with two trapped ^{111}Cd$^+$ ion qubits on the stretch mode of motion ($\omega_s = 2\pi \times 3.55$ MHz) [56]. The ground state hyperfine clock states $|F = 1, m_F = 0\rangle \equiv |1\rangle \equiv |\downarrow\rangle$ and $|F = 0, m_F = 0\rangle \equiv |0\rangle \equiv |\uparrow\rangle$ serve as qubits. The ions were initially cooled to near the ground state with Raman sideband cooling and
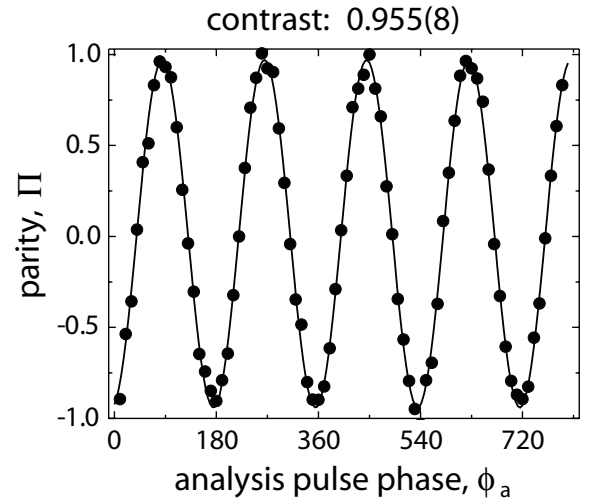

Figure 15. Parity after producing the maximally entangled state. As ϕ_a is varied, the parity of the two ions should oscillate as $\cos(2\phi_a)$ with the amplitude of oscillation equal to twice the magnitude of the density matrix element $\rho_{\downarrow\downarrow,\uparrow\uparrow}$. Each data point represents an average of 500 experimental cycles. Figure from [54]. Reprinted with permission from MacMillan Publishers Ltd, copyright (2003).
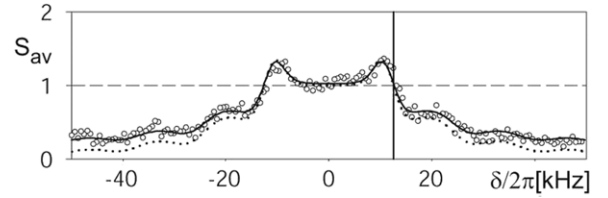

Figure 16. Average brightness S_{av} versus MS gate detuning δ. Applied gate time (75 μs) is within 10% of ideal. Dotted line indicates expected signal modified to include an initial temperature $\bar{n}_s = 0.3$ [55]. Solid line is a fit including offset and contrast factor emissions to account for imperfections such as spontaneous emission. the fit gives a sideband Rabi frequency $\eta\Omega/2\pi = 6.3$ kHz and initial stretch mode temperature $\bar{n}_s = 0.3$. Vertical line shows ideal gate operation point $\delta = 2\eta\Omega$, roughly at $S_{av} = 1$. Each point is the average of 150 PMT measurements. Figure from [56].

the electronic states were initialized through optical pumping. The gate was generated by applying a red sideband and blue sideband with equal coupling strengths and opposite detunings.

Figures 16 and 17 show the outcome of the gate pulses applied to two ^{111}Cd$^+$ on the stretch mode of motion. Figure 16 plots the average brightness S_{av} versus gate detuning δ. The vertical line indicates the ideal gate operation point which leads to maximally entangled states. Figure 17 illustrates the parity signal which allows determination of the off-diagonal elements of the density matrix. For the plot shown, the amplitude of oscillation is 0.79(2) [56]. The fidelity of this entangling gate is 83%. The main decoherence sources are fluctuating ac Stark shifts during the gate pulses and spontaneous emission caused by the Raman fields the form the gate pulses [56].

4.2. Experimental implementations of quantum algorithms

The Deutsch–Jozsa (D–J) algorithm computes whether a function is constant or balanced in a single query. An
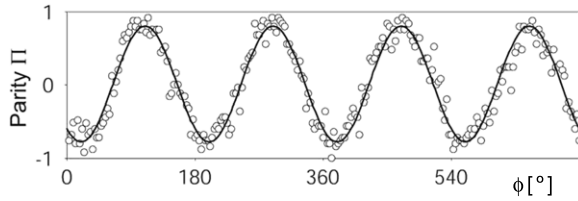
Figure 17. Parity versus phase of analysis $\pi/2$ pulse applied to the Ψ_1 state. The solid line is a sinusoidal fit yielding an amplitude 0.79(2). The fidelity of the state shown is 0.83(2). Each point is an average over 50 PMT measurements. Figure from [56].

alternative explanation is to determine whether a coin is fair, with heads on one side and tails on the other, or fake, with either heads or tails on both sides. Classically you would need to look at both sides of the coin to determine which type it was, but with the D–J algorithm only a single query is necessary.

In 2002 this algorithm was experimentally demonstrated with a single $^{40}\text{Ca}^+$ ion qubit [64]. The four qubit states are encoded in the two electronic states $|S_{1/2}, m_F = -1/2\rangle \equiv |0\rangle$ and $|D_{5/2}, m_F = -1/2\rangle \equiv |1\rangle$ and the two lowest phonon (motional) states $|n_z = 0_z\rangle \equiv |1\rangle$ and $|n_z = 1_z\rangle \equiv |0\rangle$. Qubit operations were realized with proper laser pulses, similar to the operations discussed in the previous section. Figure 18 illustrates the circuit to implement the algorithm. The four coin outcomes (both heads, both tails, head/tails, tail/heads) are represented by four functions f that map the input bit ($a = 0, 1$) corresponding to a side of the coin onto an output bit ($f(a) = 0, 1$) corresponding to heads or tails. The four possible outcomes are $f_1(a) = 0$, $f_2(a) = 1$, $f_3(a) = a$ and $f_4(a) = \bar{a}$. The first two are constant functions representing a fake coin and the last two balanced functions that represent a fair coin. Computing $f(0) \bigoplus f(1)$ yields 0 (or 1) for a constant (or balanced) function. Classically this would require two function calls, but the D–J algorithm requires only one. The experimental results are tallied in table 2 and the experimental time evolution of $|\langle 1|a\rangle|^2$ is shown in the graphs in figure 19. The value of $|\langle 1|a\rangle|^2$ determines if the function is constant or balanced [64].

Quantum teleportation could be a viable means toward scalable quantum information processing. In 2004 two groups simultaneously implemented teleportation between two trapped ion qubits [65, 66]. One experiment was carried out with trapped $^{40}\text{Ca}^+$ ions and one with $^9\text{Be}^+$ ions. For both experiments three qubits were needed; one for the sender, one for the receiver and a third ancillary bit that is maximally entangled with the receiver's qubit. In the case of two qubits, only two bits of classical information needed to be sent to transport the quantum state. In both experiments the information from one qubit was transported to a second distant qubit, but the actual physical qubits were not transported.

The first experiment was carried out on trapped $^{40}\text{Ca}^+$ ions confined in a single zone linear ion trap. The qubits consisted of the $|S_{1/2}, m_j = -1/2\rangle \equiv |1\rangle$ ground state and a metastable $|D_{5/2}, m_j = -1/2\rangle \equiv |0\rangle$ state. Figure 20 shows the circuit to implement the teleportation protocol. All three ions are cooled to near the ground state and initialized to the $|1\rangle$ state. Ions 2 and 3 are prepared in the Bell state $|\Psi_+\rangle_{23} = |0\rangle_2|1\rangle_3 + |1\rangle_2|0\rangle_3/\sqrt{2}$. Next ion 1 is prepared in an
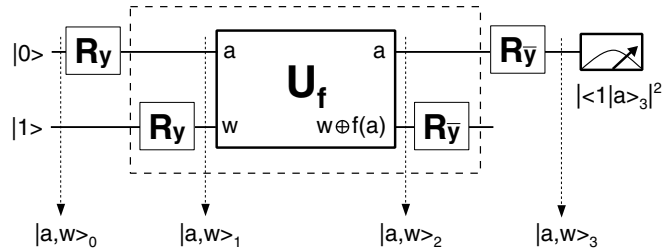

Figure 18. Quantum circuit for implementing the Deutsch–Jozsa algorithm with basic quantum operations. The upper line shows the input qubit $|a\rangle$ ('which side of the coin' information), the lower line an auxiliary working qubit $|w\rangle$ (corresponding to the channel on which the answer is provided). The rotations R_y create superpositions $|a\rangle_0 = (|0\rangle + |1\rangle)/\sqrt{2}$ and $|w\rangle_1 = (|0\rangle - |1\rangle)/\sqrt{2}$ from the inputs $|a\rangle_0 = |0\rangle$ and $|w\rangle_0 = |1\rangle$. The box U_{f_n} represents a unitary operation specific to each of the functions f_n, which applies f_n to a and adds the result to w modulo 2. Table 1 lists the logic operations required for transforming $|w\rangle$ into $|w \bigoplus f_n(a)\rangle$. The output of the box is $|a, w\rangle_2 = (|0, w_{in} \bigoplus f_n(0)\rangle + |1, w_{in} \bigoplus f_n(1)\rangle)/\sqrt{2}$. Up to an overall sign $|w\rangle$ is left unchanged, but the positive superposition $(|0\rangle + |1\rangle)/\sqrt{2}$ on $|a\rangle$ is transformed into a negative superposition $|a\rangle_2 = (|0\rangle - |1\rangle)/\sqrt{2}$ if f is balanced; otherwise it is unchanged. After the final rotations $R_{\bar{y}}$, a measurement on $|a\rangle$ is performed with result $|a\rangle_3 = $ either $|0\rangle$ or $|1\rangle$. Because of the sing change in $|a\rangle_2$ if f is balanced, $|\langle 1|a\rangle_3|^2 = f_n(0) \bigoplus f_n(1)$, that is, $|a\rangle_3$ yields the desired information whether the function f_n is balanced or constant. The working qubit w resumes its initial value $|w\rangle_3 = |w\rangle_0 = |1\rangle$. Figure from [64]. Reprinted with permission from MacMillan Publishers Ltd, copyright (2003).

arbitrary state $|\chi\rangle$, which was one of the four non-orthogonal test states: $|\chi^{(1)}\rangle = |1\rangle$, $|\chi^{(2)}\rangle = |0\rangle$, $|\chi^{(3)}\rangle = (|0\rangle + |1\rangle)/\sqrt{2}$, $|\chi^{(4)}\rangle = (i|0\rangle + |1\rangle)/\sqrt{2}$. A Bell-state analysis (which includes a controlled-phase entangling gate) is performed followed by a $\pi/2$ pulse on each ion. In the last step, the joint quantum state of ions 1 and 2 is measured. Prior to this step the state of ion 3 is transferred to a superposition of states that remain unaffected by the detection pulses in order to preserve the coherence [65].

Figure 21 shows the teleportation outcome. The gray shaded bars show the four states that were transported with fidelities of 76%, 74%, 73% and 75%. The unshaded bars illustrate the outcome if the reconstruction operations are not performed, in this case the average fidelity is 49.6%. The largest error sources come from unstable magnetic fields and laser-frequency noise [65].

In the second experiment three trapped $^9\text{Be}^+$ confined in a multi-zone ion trap were teleported [66]. Unlike the previous experiment, the ions were trapped in a multi-zone rf-linear Paul trap with eight segmented electrodes. This allowed for multiple trapping zones and made it possible to separate the qubits during operations. The qubit levels were the ground state hyperfine levels $|F = 1, m_F = -1\rangle \equiv |\uparrow\rangle$ and $|F = 2, m_F = -2\rangle \equiv |\downarrow\rangle$ and single qubit and entangling interactions between the qubits were accomplished through stimulated Raman transitions, as previously discussed. Figure 22 illustrates the steps of the protocol. The ions were initialized to the $|S\rangle_{1,3} \otimes |\downarrow\rangle_2$ state, where $|S\rangle_{1,3} \equiv |\uparrow\rangle_1|\downarrow\rangle_3 - |\downarrow\rangle_1|\uparrow\rangle_3$. The first step in the teleportation process is to implement a Bell-state measurement on ions 1 and 2,
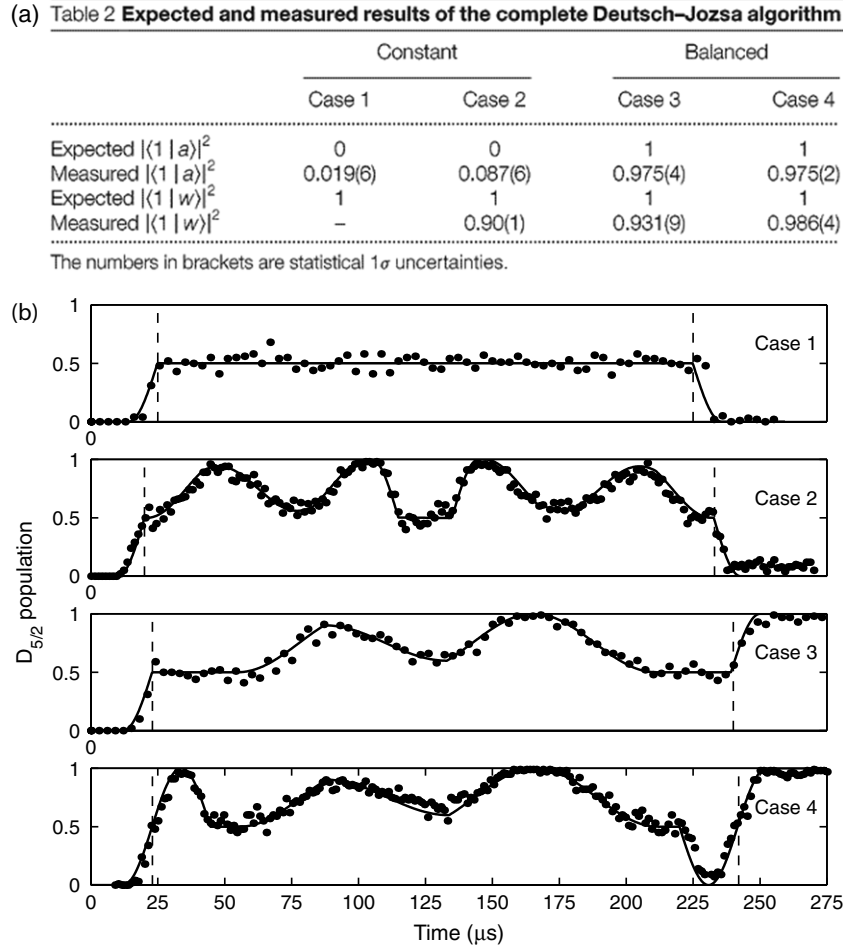
(a) Table 2 **Expected and measured results of the complete Deutsch–Jozsa algorithm**

	Constant		Balanced	
	Case 1	Case 2	Case 3	Case 4
Expected $|\langle 1 | a \rangle|^2$	0	0	1	1
Measured $|\langle 1 | a \rangle|^2$	0.019(6)	0.087(6)	0.975(4)	0.975(2)
Expected $|\langle 1 | w \rangle|^2$	1	1	1	1
Measured $|\langle 1 | w \rangle|^2$	–	0.90(1)	0.931(9)	0.986(4)

The numbers in brackets are statistical 1σ uncertainties.

Figure 19. (a) Table displaying expected and measured results of the complete Deutsch–Jozsa algorithm. (b) Time evolution $|\langle 1|a\rangle|^2$. Points are the probabilities, each inferred from 100 measurements, the line shows the ideal evolution. No parameters were adjusted to fit the data. the implementation of the functions $R_{\bar{y}_w} U_{f_n} R_{y_w}$ takes place between the dashed lines. An initial R_{y_a} and a final $R_{\bar{y}_a}$ rotation on $|a\rangle$, implemented by carrier pulses, complete the algorithm. Taking case 3 as an example, R_{y_a} lasts from 12 to 22 μs. Then $R_{\bar{y}_w} U_{f_n} R_{y_w}$ on $|a, w\rangle$ is implemented from 54 to 212 μs with the laser tuned to the blue sideband. The laser phase is switched at 87, 133 and 166 μs. The final $R_{\bar{y}_a}$ pulse is applied from 240 to 250 μs. Figure from [64]. Reprinted with permission from MacMillan Publishers Ltd, copyright (2003).
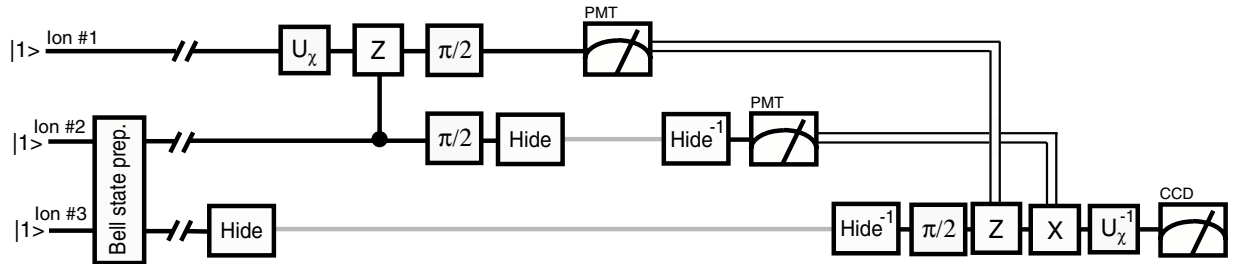

Figure 20. Teleportation from ion 1 to ion 3. A Bell state of ions 2 and 3 is prepared as a resource. The state to be teleported in encoded in ion 1 by the operation U_χ. The Bell-state analyzer consists of a controlled-Z gate followed by $\pi/2$ rotations and a state detection of ions 1 and 2. Note that this implementation uses a Bell basis rotated by $\pi/4$ with respect to the standard notation. Therefore, a $\pi/2$ rotation on ion 3 is required before the reconstruction operations Z and X. The latter operations are realized by a π rotation around the z and x axes, respectively. Gray lines indicate qubits that are protected against light scattering. Ions 1 and 2 are detected by observing their fluorescence on a photomultiplier tube (PMT). Only on a detection event $|0\rangle$ is the corresponding reconstruction operation applied to ion 3. Classical information is represented by double lines. For the fidelity analysis we apply U_x^{-1}, and measure the quantum state of ion 3 by observing its resonance fluorescence using a CCD camera. Figure from [65]. Reprinted with permission from MacMillan Publishers Ltd, copyright (2004).

this is done by separating the three ions in different trapping regions. Ion 3 is held is section 7 while ions 1 and 2 are confined in section 5. A phase gate is applied to the ions, using the σ_z coupling discussed above, followed by a $\pi/2$

pulse. After this, all three ions are recombined and ion 1 is shuttled to trap 5 for detection while ions 2 and 3 are confined in trap 7. The ions are once again combined in trap 6 and then separated with ions 1 and 2 confined in trap 5 and ion 3
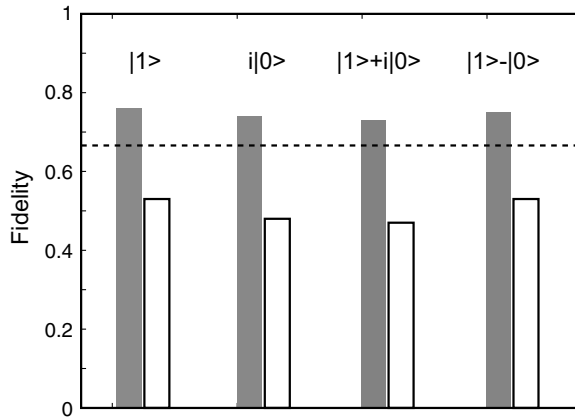
Figure 21. Result of the teleportation. The four test states are teleported with fidelities of 76%, 74%, 73% and 75%, respectively (gray bars). For each input state, 300 single teleportation experiments were performed. The error of each entry, estimated from quantum projection noise, is 2.5%. For comparison, white bars show the results if the reconstruction operations are omitted, yielding an average fidelity of 49.6%. The optimum 'teleportation' obtainable by purely classical means reaches a fidelity of 66.7% (dashed line). Figure from [65]. Reprinted with permission from MacMillan Publishers Ltd, copyright (2004).
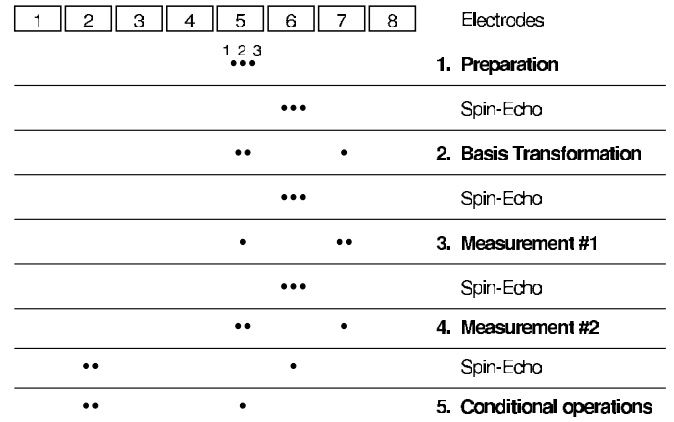

Figure 22. Schematic representation of the teleportation protocol. The ions are numbered left to right, as indicated at the top, and retain their order throughout. Positions, relative to the electrodes, are shown at each step in the protocol. The widths of the electrodes vary, with the width of the separation electrode (6) being the smallest at $100\,\mu$m. The spacing between ions in the same trap is about $3\,\mu$m, and the laser beam spot sizes (in traps 5 and 6) at the position of the ions are approximately $30\,\mu$m. In step 1 we prepare the outer ions in an entangled (singlet) state and the middle ion in an arbitrary state (equation (1)). Steps 2–4 constitute a measurement in a Bell basis for ions 1 and 2, teleporting the state of ion 2 onto ion 3, up to unitary operations that depend on the measurement outcomes. In step 5 these conditional operations are invoked, recovering the initial state. Interspersed are spin-echo pulses applied in trap 6 that protect the state from dephasing due to fluctuating magnetic fields but do not affect the teleportation protocol. Figure from [66]. Reprinted with permission from MacMillan Publishers Ltd, copyright (2004).
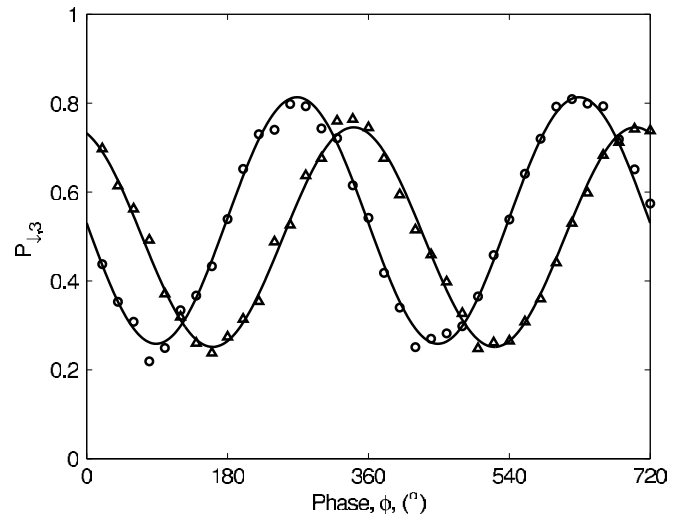
in trap 7. The spin echo before this step transferred the state of ion 1 to the $|\uparrow\rangle_1$ state, so now when both ions 1 and 2 are simultaneously detected, the state of ion 2 is well known. Lastly unitary operations are applied to ion 3 that are dependent on the measurement outcomes of ions 1 and 2. Figure 23 illustrates Ramsey fringes for the teleportation protocol for the basis states $|\uparrow\rangle_2$ and $|\downarrow\rangle_2$. For this Ramsey experiment the first $\pi/2$-pulse is applied to ion 2 and the second pulse is applied to ion 3 after the teleportation protocol is implemented. An average fidelity of 78% is achieved. The main error sources are imperfect initialization to the $|S\rangle_{1,3}\otimes|\downarrow\rangle_2$ state, imperfections in the second phase gate due to heating during transport to different trapping zones, and dephasing due to fluctuating magnetic fields [66].

The quantum discrete Fourier transform (QFT) may be one of the most powerful tools in quantum computing in the sense that it is responsible for the exponential speed up over many classical algorithms. It is a key step in Shor's factoring algorithm where it is used to find the period in a set of quantum amplitudes during the algorithm's order-finding subroutine. In addition, the QFT is used for phase estimation and the discrete logarithm [3]. In 2005 a semiclassical QFT was implemented with trapped ^{9}Be$^+$ ions [67]. Although not as powerful as the discrete QFT, the semiclassical QFT is still useful. In the semiclassical QFT each qubit is measured and then controlled-phase rotations are applied to the remaining qubits dependent on the classical measurement outcomes. No entangling gates are necessary to carry out the semiclassical QFT, and so, the requirements over the ion's motional states are considerably reduced [67]. Despite the lack of entangling gates, this algorithm is an important step toward creating a fully coherent QFT in a trapped ion system which is a necessary condition for realizing Shor's factoring algorithm.

The experiment was carried out with three trapped ^{9}Be$^+$ ions in a set-up similar to the second teleportation experiment

Figure 23. Ramsey fringes demonstrating the teleportation protocol. The two curves correspond to the second Ramsey pulse having $\phi_{\text{fixed}} = 0$ (circles) and $\phi_{\text{fixed}} = \pi/2$ (triangles) as discussed in the text. We plot the probability $P_{\downarrow,3}$ of observing ion 3 in the $|\downarrow\rangle_3$ state versus the phase of the first Ramsey pulse. Solid curves are best-fit sinusoidal functions to the data. The oscillations of the Ramsey fringes have an amplitude $|\rho_{\downarrow\uparrow}|$ where $\rho_{\downarrow\uparrow} = (\rho_{\downarrow\uparrow})^*$ is the off-diagonal element of the density matrix of the teleported state. The fidelity of the teleported state is then given by $F = 1/2 + |\rho_{\downarrow\uparrow}|$. Figure from [66]. Reprinted with permission from MacMillan Publishers Ltd, copyright (2004).

described above [67]. The period finding algorithm was tested on five different states with periods 1, 2, 4, 8 and approximately 3. Eight states are possible with three qubits: $|000\rangle$, $|001\rangle$, $|010\rangle$, $|100\rangle$, $|101\rangle$, $|110\rangle$, $|011\rangle$ and $|111\rangle$.
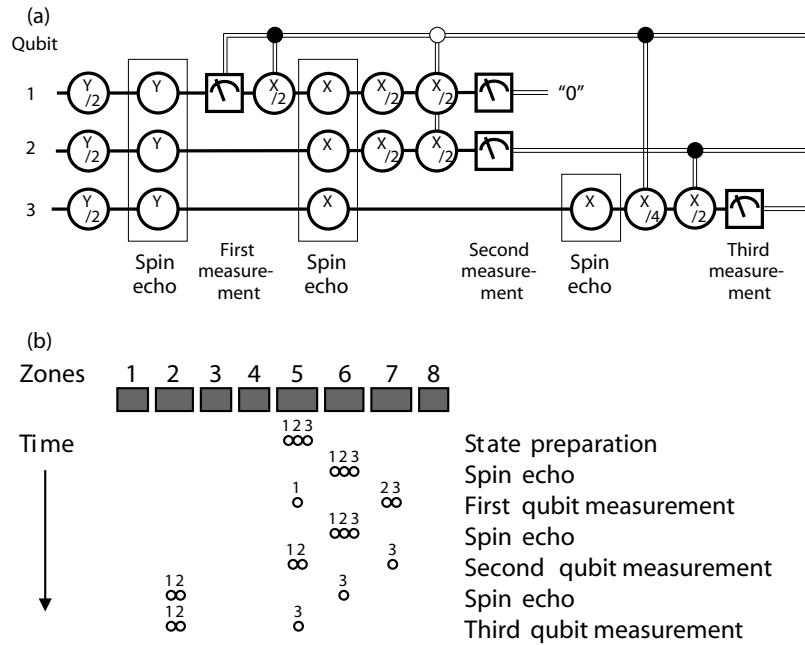
Figure 24. Circuit for the QFT and locations of the ions in the multi-zone trap during protocol execution. (*a*) The semiclassical QFT [68] as implemented in this experiment. The double lines denote classical information. The closed circles on control lines denote rotation conditional on '1'; the open circles denote rotation conditional on '0'. The initial conditional rotation of qubit 1 ensures that is is in the nonfluorescing state when the second ion is measured (the second ion is measured in the presence of the first ion, which contributes negligibly to the fluorescence signal during the second measurement [69]; refer to 'Second qubit measurement' in (*b*)). This circuit, up to some irrelevant phases, can be obtained from the circuit for the quantum Fourier transform of three qubits [3] through conjugation of rotations and reordering of some operations. (*b*) The locations of the ions in the mulitzone trap structure during the QFT protocol as a function of time. Separation of ions and refocusing operations are preformed in zone 6, and all other qubit operations are preformed in zone 5. Figure from [67]. Reprinted with permission from AAAS.

The recurrence of quantum amplitudes in a superposition of these eight states results in periodicities. Figure 24 illustrates the circuit for the algorithm. The algorithm started with all three ions cooled to the ground state of motion and initialized to the $|111\rangle$ state. One of the five input states was created with additional rotations and then several thousand implementations of the QFT protocol were carried out. The steps are (i) rotation of ion 1, (ii) measurement of ion 1, (iii) rotation of ion 2 conditional on measurement of ion 1, (iv) measurement of ion 2, (v) rotation of ion 3 conditional on the first 2 measurements and (vi) measurement of ion 3 [67]. Figure 25 shows the experimental outcome and theory prediction for each of the five cases. Each plot is the measured probability versus the output state 0–7. The differences between theory and experiment are explained by systematic errors in the experiment. The systematic errors include imperfect state preparation, separate detections of the qubits at different times and conditional rotations of the ions. The former is not associated with the QFT protocol but the latter two are intrinsic to the protocol. For this system slow magnetic field fluctuations caused dephasing errors for the detection of each qubit. Despite these noise sources, the experimental states still had significant squared statistical overlap with theory predictions, proving that, even with large error sources, the semiclassical QFT does a good job at period finding [67].

The last algorithm we will discuss is Grover's quantum database search algorithm. This algorithm is intended to search an unsorted database with polynomial speed up over classical methods. A common analogy for the algorithm is to find a person's name in the phone book given only their phone number [70]. To find a person's phone number given only their name is a trivial task since the phone book is ordered alphabetically. However, searching the other way is a much more difficult problem because now the phone book becomes an unsorted database. Given this problem one would have to search half the phone book, on average, classically. However, if you could implement Grover's algorithm then the average search is reduced to $\sqrt{N}$ queries instead of the $N/2$ queries required classically. Although this is not the exponential speed up of Shor's algorithm, this algorithm may be more adaptable because it can provide polynomial speed up to almost any quantum algorithm [71].

The power behind this algorithm lies in the 'oracle query' function. The oracle can recognize whether or not input x is a solution to the given problem. In practice, the oracle function marks a specific state by flipping the state's sign so that when the remaining operations in the algorithm are performed, the amplitude of the marked state increases while the amplitude of the unwanted states decreases. Upon measurement, the probability of finding the marked state is much higher than any other element of the database. In the full algorithm the oracle would itself have to be a quantum database, but for the purpose of this demonstration it is considered a black box that performs the function $|x\rangle \rightarrow -|x\rangle$.

This proof of principle experiment was conducted with two trapped $^{111}Cd^+$ qubits giving a four element database [72].
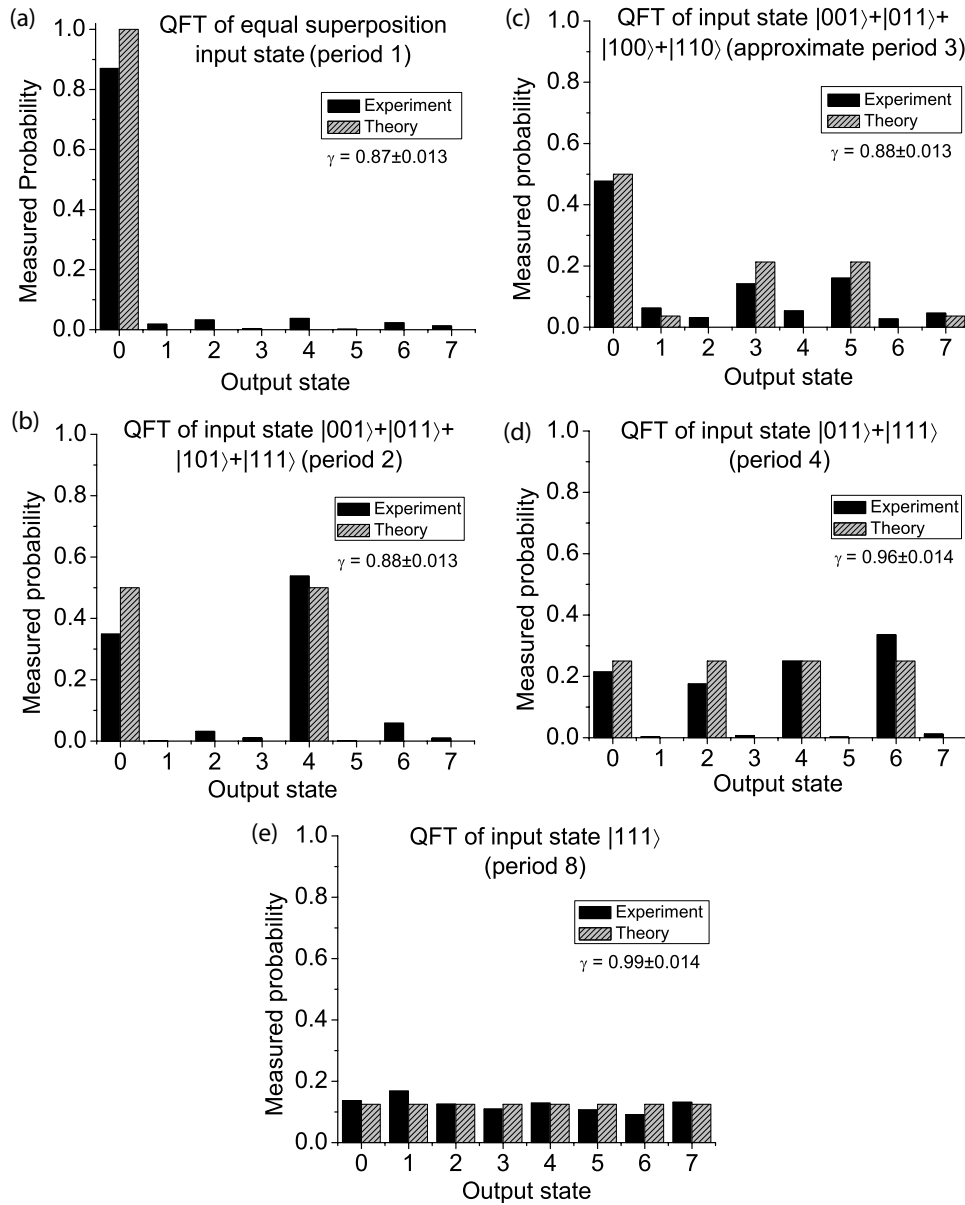
Figure 25. Results of the semiclassical QFT. Measured probability of each output state occurring after the application of the protocol shown along with the expected transform output. Each plot contains data from 5000 experiments. The SSO γ is a measure of the transform accuracy. Uncertainties quoted for the SSO are statistical and do not include systematic errors. (*a*)–(*e*) are the QFTs for $|\Psi_1\rangle$, $|\Psi_2\rangle$, $|\Psi_3\rangle$, $|\Psi_4\rangle$, and $|\Psi_8\rangle$, respectively. Figure from [67]. Reprinted with permission from AAAS.

The qubit levels are the magnetic field insensitive ground state hyperfine levels $|F = 0, m_F = 0\rangle$ and $|F = 1, m_F = 0\rangle$. In this scalable demonstration magnetically insensitive 'clock state' qubits are used, as well as a configuration of the σ_x gate that is insensitive to external phase drifts between gates [50, 55, 56].

Figure 26 illustrates a general overview of the algorithm for an arbitrary sized database. The first step is to initialize all the database elements to a known state, in this case the $|0\rangle^{\otimes n}$ state. Here the $(|xx\rangle^{\otimes n})$ denotes that $|xx\rangle$ is tensored with itself n times. A Hadamard gate is applied to put all of the database elements in an equal superposition, this makes all possibilities equally likely. Applying the oracle flips one of the database elements by 180°, as shown in figure 26(*b*). Two more Hadamard gates surrounding a phase gate implement the state amplification process, which increases the weighting of

the marked state. The entire algorithm, from the oracle query on, is repeated for the integer closest to $(\frac{\pi \sin(N^{-1/2})}{4} - 1/2)$ times [73], for $N \gg 1$ this is approximately $\pi\sqrt{N}/4$ times. If the algorithm is repeated too many times, then the weighting of the marked states begins to decrease while the weighting of the unwanted states increases. It is interesting to note that for four database elements, the marked state can be recovered with 100% probability.

Figure 27 shows the experimental circuit to implement the algorithm for $N = 4$ search elements in the trapped ion system. The ions are first prepared in the $|0\rangle|0\rangle$ state. A $\pi/2$ prepares the ions in the equal superposition state $\frac{1}{\sqrt{2}}(|0\rangle|0\rangle + |0\rangle|1\rangle + |1\rangle|0\rangle + |1\rangle|1\rangle)$, this pulse results in the same operation as the Hadamard gate in figure 26 and the resulting state is schematically shown in figure 26(*a*). The oracle function is
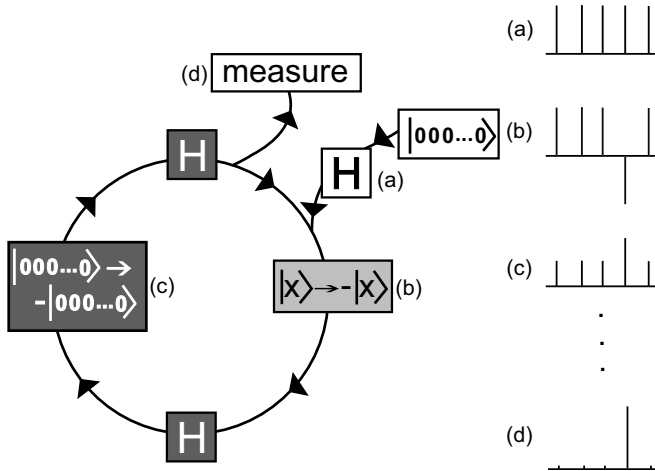
Figure 26. Schematic diagram of Grover's quantum search algorithm over a space of n qubits ($N = 2^n$ entries). Initially, all qubits are prepared in the state $|000...0\rangle$. (a) A global Hadamard gate prepares an equal superposition of all states. (b) The oracle (shaded in light gray) flips the sign of the amplitude corresponding to the marked element, represented by the n-bit binary number x. (c) Two global Hadamard gates surround an additional phase gate (shaded in dark gray) that flips the sign of the amplitude corresponding to the initial state $|000...0\rangle$, amplifying the weight of the marked state. Steps (b) and (c) are repeated in sequence a prescribed number of times, and finally (d) the qubits are measured. An example of the distributions of quantum amplitudes at each stage are depicted at the right. Figure from [72].

realized by creating a controlled-z gate from the σ_x entangling gate, denoted by G_{MS} in the figure. This is accomplished by applying the single qubit rotations (boxed in white inside the gray-shaded box) in figure 27 before and after the σ_x gate. These operations transform the $|11\rangle$ state to the $-|11\rangle$ state. The black shaded boxes allow one to move the minus sign around to any of the four database elements because, for the oracle query to be effective, we need to be able to mark any of the four states and not just the $|11\rangle$ state. These are differential single qubit rotations that allow the qubits to be rotated 90° out of phase with each other. The angles α and β determine which database element is marked. For example, to mark the $|01\rangle$ state the rotations $R(\pi, \pi)$ and $R(0, 0)$ would be applied to qubits 1 and 2, respectively, before the controlled-z gate is applied. After the controlled-z gate, the rotations $R(\pi, 0)$ and $R(0, 0)$ would be applied to the qubits 1 and 2, respectively. This sequence of rotations performs the operation

$$\begin{bmatrix} 1 & 0 & 0 & 0 \\ 0 & -1 & 0 & 0 \\ 0 & 0 & 1 & 0 \\ 0 & 0 & 0 & 1 \end{bmatrix} \quad (19)$$

and takes the state prior to entering the oracle, $\frac{1}{\sqrt{2}}(|00\rangle + |01\rangle + |10\rangle + |11\rangle)$, to the state $\frac{1}{\sqrt{2}}(|00\rangle - |01\rangle + |10\rangle + |11\rangle)$ directly following the oracle. Any of the four states could be marked in a similar fashion. The final entangling gate and single qubit rotations perform the state amplification process. For this case where the $|01\rangle$ state is marked, after the entangling gate the state of the system is $0|00\rangle + 1|01\rangle + 0|10\rangle + 0|11\rangle$. All of

the population is rotated into the $|01\rangle$ state and this state will be measured with 100% probability. This is a result of the interference between the entangling gate inside the oracle and state amplification process. This is the powerful phenomena that Deutsch recognized in 1985 [5, 6].

Figure 28(a) shows the results of the algorithm. The states on the right-hand side of the graph are the state marked by the oracle and the graphs show the measured states. The marked state was recovered with 60% probability, on average. This considerably lower than the 100% possible for a four element database. This discrepancy is due to imperfections in the circuit. Each instance of the entangling gate has a fidelity of 80%, and since there are two entangling gates in the circuit, the best possible fidelity for this implementation could be 64%. As stated earlier, the main sources of decoherence during the gate are spontaneous emission from off-resonant coupling to the excited state and fluctuating ac Stark shifts from the Raman beams that drive the entangling gate [56]. Both of these can be reduced by increasing the detuning from the excited state during the gate operation. However, in this Cd ion system the total power is limited to only a few milliwatts due to the technical difficulties in generating 214 nm light. This detuning was chosen to give a reasonable gate speed as well as minimize the spontaneous emission rate. If more power was available, the detuning could be increased while maintaining a reasonable gate speed, and the gate fidelity could be much higher (see [56] for more details). One other source of error arises from ac Stark shifts during the differential single qubit rotations in the oracle query. It is estimated that this causes infidelities of roughly 5–10%.

The desired states (equation (18)) are produced with a fidelity of approximately 80%. For this implementation the phases ϕ_0, ϕ_{s1} and ϕ_{s2} are fixed before running the experiment by synchronizing the phase of the entangling gate to that of the microwave $\pi/2$ pulses [55] and then the two gates are synchronized to each other with a Ramsey experiment. This reduces the gate to a σ_x coupling. The entire algorithm takes 20 pulses and $\sim$380 μs to complete, with the σ_x gates being the most time consuming operations [72].

Classically, Grover's algorithm is similar to a shell game where a marble is hidden under one of four shells and the participant is given one oracle query before guessing the location of the marble. In this way, the best classical outcome is 50% since there is a 25% chance for the query to give the correct location and 75% of the time the participant will need to choose from the remaining three choices giving $P_{cl} = 1/4 + 3/4(1/3) = 0.50$. For Grover's algorithm, in an ideal case, the marble can be found in a single guess. In this way the classical limit was surpassed in this experiment as the marked state was recovered with an average probability of 60%.

Figure 28(b) shows the results of the algorithm with the final entangling gate omitted. In this case, the oracle is considered a black box function. The graphs show that the marked state is only recovered with an average probability of 42%, meaning that without entanglement, quantum superposition can do no better than classical means. This also allows us to determine the fidelity of the oracle operation. Since the rotations after the oracle create a Bell
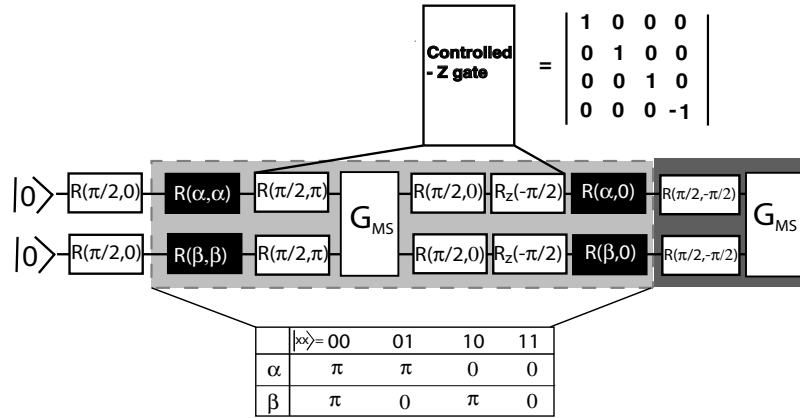
Figure 27. The experimental circuit to implement the algorithm for $n = 2$ qubits, where $R(\theta, \phi)$ is a rotation on the Bloch sphere, $R_z(\phi)$ is a phase rotation about the $\hat{z}$-axis, and G_{MS} is the σ_x entangling gate. The light gray-shaded box identifies the oracle, where the value of the variables α and β (given in the table), determine which state is marked . The rest of the circuit (shaded in dark gray) amplifies the weighting of the marked state. The final step is to detect the ions with a CCD camera. For this algorithm a CCD camera must be used since the spatial information to distinguish the bright/dark from the dark/bright state is necessary. Figure from [72].

state, there is a maximum probability of 50% to recover the marked state. The data show that the marked state was recovered with 42% probability, on average, inferring a fidelity of roughly 80% for the oracle.

Another useful measure to gauge an algorithm's success is the mutual information that was discussed in section 2. The mutual information between the marking of the state and the measurement can be used to characterize the information content in the distributions. Classically the mutual information acquired after a single query of the oracle is $H(x : y) = 0.25 \log_2(0.25) - 0.75 \log_2(0.75) = 0.81$ bits, meaning, on average, 0.81 bits of information are gained upon measurement. The ideal quantum algorithm would yield two bits of information upon measurement. For the data in figure 28(a) the mutual information is 0.44, so on average only about a half a bit of information is gained. Even though less information is gained per measurement than the classical case, the *probability* of finding the marked state in the experiment still exceeds the classical limit.

This section has reviewed the major entangling gate schemes and quantum algorithms implemented with phonon-mediated entangling gates in trapped ion systems over the last decade. More recently, researchers have entangled up to eight ions and have pushed the fidelities of the above entangling gates on a few ions past the 95% level [74–76]. A three qubit Toffoli gate was recently demonstrated [77] and newer theories are appearing for better ways to entangle ions, one in particular is to use magnetic fields to drive entangling gates instead of electric fields [78]. This moves the field ever closer to fabricating a scalable quantum computer capable of realizing nontrivial algorithms.

5. Outlook

Over the last 15 years trapped ion experiments have realized all of the basic requirements to fabricate a quantum computer. Trapped ions possess an unparalleled level of control and coherence compared with other systems. Small algorithms have been achieved and entanglement fidelities are now well above 95% for small numbers of ions [15, 76].

The biggest challenge left for ion traps is to scale up to a higher number of qubits. This will require more complex trap structures that have different zones for trapping, logic operations and storage [46]. Currently, researchers are approaching this goal from a few different directions. One route is to make three-layer traps, similar to the one shown in figure 2(c), but instead of one trapping zone the newer traps have multiple trapping regions through which the ions can be shuttled for various qubit operations. Although these traps have been fabricated and demonstrated to work [15], there is a high degree of difficulty in physically making all of the connections, and this only becomes more tedious as the number of electrodes increases. An easier approach is to use microelectromechanical systems (MEMS) technology as the ion trap can be etched from a single grown semiconductor structure [79, 60, 61]. This alleviates the need to laser machine and hand align separate layers and also allows for a faster trap turn around time since only the etching mask needs to be changed in order to fabricate a new trap geometry. Future traps may also employ integrated optics for directing laser beams to the various trap regions as well as optical interconnects to couple distant ion collections [80–81]. Although one of the concerns that arises with these smaller trapping structures is unwanted ion heating. As the ion traps become smaller closer attention will have to be paid to prevent heating of the ions due to fluctuating patch potentials that were previously discussed (see section 3.7).

To date trapped ion quantum computers have demonstrated approximately fifty coherent operations. Although this is enough to show proof of principle experiments, it is not enough to show scalable non-trivial quantum computations. A fully operational quantum computer capable of solving classically intractable problems would require thousands of qubits and on the order of one million qubit operations. A big step in this process is the ability to implement error correction protocols. Error correction involves encoding the physical qubit's information in a redundant way, such that if there is an error, the original information can be recovered (decoded) [3]. Fault-tolerant quantum computing sets an error threshold, and as long as the individual operations remain below this threshold, the
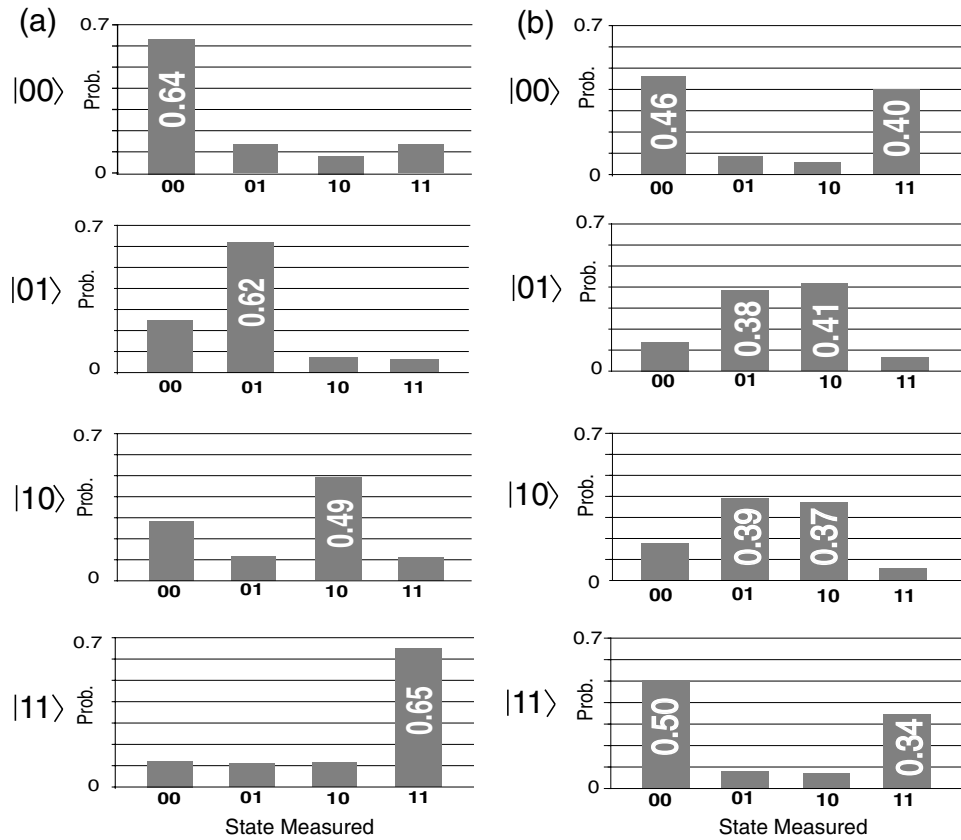
Figure 28. (*a*) Output of the algorithm. The conditional probability of measuring each of four output states given one was marked is shown in sequence from top to bottom $|00\rangle$, $|01\rangle$, $|10\rangle$, $|11\rangle$. Each of the four data sets shows the distribution of measurements averaged over 500 trials. The marked state was recovered on average with 60(2)%, compared with unit probability for the ideal quantum algorithm and 50% for the best possible classical algorithm. (*b*) Output of the algorithm without the final entangling gate. This shows that the fidelity of the oracle is about 80%. Each of the four data sets was also averaged over 500 trials. The experimental average to recover the marked state is 41(2)% with the theoretical limit of 50%, both of which are less than the 60% from (*a*). The quoted errors are statistical. Figure from [72].

computation will be successful. It is expected that error thresholds between 10^{-4} and 10^{-2} will be necessary for fault-tolerant computing [82–84]. Recently, experimentalists at the University of Innsbruck implemented a M–S gate approaching fault-tolerant limits with a fidelity of 99.3(1)% [76]. Other recent experiments show that error correction protocols are possible, and though not yet at the fault-tolerant limit, it is a feasible goal in the near future [85]. In the mean time, trapped ion quantum computers with their current capabilities may lend themselves to other applications.

One ground breaking application of ion trap quantum computing is to use quantum logic spectroscopy for an atomic clock [86]. It has long been thought that ^{27}Al$^+$ would be a good atomic clock standard because of the narrow transition linewidths and small systematic shifts of the triplet P states. However, the unfavorable transition between the $^1S_0$ and $^1P_1$ states at 167 nm makes laser cooling and detection difficult as this is a arduous color of light to generate. Recently, researchers at NIST in Boulder, CO have used entanglement between a trapped ^{9}Be$^+$ ion and a trapped ^{27}Al$^+$ ion to cool, initialize, and readout information in the ^{27}Al$^+$ ion to produce an atomic clock that rivals the current Cs time standard [87]. Using the collective motional mode to entangle the ^{9}Be$^+$ and ^{27}Al$^+$ ions, they were able to show a fractional uncertainty of 5.2×10^{-17} in the ratio between a Hg$^+$ and Al$^+$ atomic clock.

The ratio had to be taken with respect to the a Hg$^+$ ion clock because the current Cs atomic clock is limited to an uncertainty of 3.3×10^{-16} [87].

Perhaps the most immediately significant application of trapped ion quantum computing is for quantum simulation (QS). Quantum simulation was first introduced by Richard Feynman in 1982 [4] and proved possible about 10 years later by Seth Lloyd [88]. In quantum simulation one well controlled, well understood quantum system is used to simulate another, more complicated quantum system. QS on a classical computer would require exponential resources, but for a quantum computer the necessary resources are proportional to the number of variables being simulated, this holds as long as the interactions are local [88]. QS is an intriguing field of study right now because the requirements to implement a simulation are considerably reduced compared with quantum computing (QC). Unlike QC, QS does not require operations to be completely coherent, nor does it require precise phase knowledge of the qubits between operations. In fact, a QS is possible with only tens or hundreds of operations and not the millions needed for QC. At the present time, this is easily within reach for trapped ion quantum computing experiments. Trapped ions have the advantage that, even though the ions are confined in a linear chain, any distant ions can be coupled through the collective motional mode and the system is not

limited to nearest neighbor interactions. Even with only a few trapped ions, fundamental unsolved problems such as magnetic frustration can be simulated [89, 90]. Research in this area could lead to revolutionary discoveries about currently unknown, and impossible to simulate classically, condensed matter phenomena such as magnetism, high temperature superconductors and supersolids.

References

[1] Shannon C E 1948 A mathematical theory of communication *Bell Syst. Tech. J.* **27** 379–423, 623–656f

[2] Turing A M 1936 On computable numbers, with an application to the entscheidungsproblem *Proc. Lond. Math. Soc. 2* **42** 230

[3] Nielsen M A and Chuang I L 2000 *Quantum Computation and Quantum Information* (Cambridge: Cambridge University Press)

[4] Feynman R P 1981 Simulating physics with computers *Int. J. Theor. Phys.* **21** 467–88

[5] Deutsch D 1985 Quantum-theory, the Church–Turing principle and the universal quantum computer *Proc. R. Soc. Lond. Ser. A—Math. Phys. Eng. Sci.* **400** 97–117

[6] Deutsch D and Jozsa R 1992 Rapid solution of problems by quantum computation *Proc. R. Soc. Lond. A—Math. Phys. Eng. Sci.* **439** 553–8

[7] Shor P W 1997 Algorithm for fast factoring *SIAM J. Comput.* **26** 1484

[8] Shor P W 1995 Scheme for reducing decoherence in quantum computer memory *Phys. Rev.* A **52** R2493–6

[9] Steane A 1996 Error correcting codes in quantum theory *Phys. Rev. Lett.* **77** 793–6

[10] Shor P W 1996 Fault-tolerant quantum computation *Proc. 37th Annu. Symp. of Fundamentals of Computer Science (Burlington, VT, Oct. 1996)* pp 56–65

[11] Cirac J I and Zoller P 1995 Quantum computation with cold, trapped ions *Phys. Rev. Lett.* **74** 4091–4

[12] Monroe C, Meekhof D M, King B E, Itano W M and Wineland D J 1995 Demonstration of a fundamental quantum logic gate *Phys. Rev. Lett.* **75** 4714–7

[13] Divincenzo D P 2000 The physical implementation of quantum computation *Fortschr. Phys.* **48** 771–83

[14] Monroe C 2002 Quantum information processing with atoms and photons *Nature* **416** 238–46

[15] Wineland D and Blatt R 2008 Entangled states of trapped atomic ions *Nature* **453** 1008–14

[16] Vidal G and Werner R F 2002 Computable measure of entanglement *Phys. Rev.* A **65** 032314

[17] Eisert J and Plenio M B 1999 A comparison of entanglement measures *J. Mod. Opt.* **46** 145

[18] Peres A 1996 Separability criterion for density matrices *Phys. Rev. Lett.* **77** 1413

[19] Horodecki M, Horodecki P and Horodecki R 1996 Separability of mixed states: necessary and sufficient conditions *Phys. Lett.* A **223** 1

[20] Wootters W K 1998 Entanglement of formation of an arbitrary state of two qubits *Phys. Rev. Lett.* **80** 2245–8

[21] Hill S and Wootters W K 1997 Entanglement of a pair of quantum bits *Phys. Rev. Lett.* **78** 5022–5

[22] Šašura M and Bužek V 2002 Cold trapped ions as quantum information processors *Phys. Rev. Lett.* **49** 1593–647

[23] Leibfried D, Blatt R, Monroe C and Wineland D 2003 Quantum dynamics of single trapped ions *Rev. Mod. Phys.* **75** 281–324

[24] Paul W, Osberghaus O and Fischer E 1958 *Forsch. Wirtsch. Verkehrsminist. Nordrhein-Westfal.* **415** 1

[25] Dehmelt H G 1962 Paramagnetic resonance reorientation of atoms and ions aligned by electron impact *Phys. Rev.* **103** 1125

[26] Dehmelt H G 1967 Radiofrequency spectroscopy of stored ions: I. Storage *Adv. At. Mol. Phys.* **3** 53–72

[27] Paul W 1990 Electromagnetic traps for charged and neutral particles *Rev. Mod. Phys.* **62** 531–40

[28] Jefferts S R, Monroe C, Barton A S and Wineland D J 1995 Paul trap for optical frequency standards *IEEE Trans. Instrum. Meas.* **44** 148

[29] Wineland D J and Itano W M 1979 Laser cooling of atoms *Phys. Rev.* A **20** 1521–40

[30] Madsen M 2006 Advanced ion trap development and ultrafast laser-ion interactions *PhD Thesis* The University of Michigan

[31] Roos Ch, Zeiger Th, Nägerl H C, Eschner J, Leibfried D, Schmidt-Kaler F and Blatt R 1999 Quantum state engineering on an optical transiton and decoherence in a Paul trap *Phys. Rev. Lett.* **83** 4713

[32] Barton P A, Donald C J S, Lucas D M, Steane A M and Stacey D N 2000 Measurement of the lifetime of the 3d $^2D_{5/2}$ state in $^{40}Ca^+$ *Phys. Rev.* A **62** 032503

[33] Wunderlich Chr, Hannemann Th, Körber T, Häffner H, Roos Ch, Hänsel W, Blatt R and Schmidt-Kaler F 2005 Robust state preparation of a single trapped ion by adiabatic passage arXiv:quant-ph/0508159v1

[34] McDonnell M J, Stacey J-P, Home J P, Ramos A, Lucas D M, Stacey D N and Steane A M 2004 High-efficiency detection of a single quantum of angular momentum by suppression of optical pumping *Phys. Rev. Lett.* **93** 153601

[35] Nägerl H C, Roos Ch, rhode H, Thalhammer G, Eschner J, Schmidt-Kaler F and Blatt R 2000 Investigating a qubit candidate: Spectroscopy on the $S_{1/2}$ to $D_{5/2}$ transition of a trapped calcium ion in a linear Paul trap *Phys. Rev.* A **61** 023405

[36] Schmidt-Kaler F, Gulde S, Riebe M, Deuschle T, Kreuter A, Lancaster G, Becher C, Eschner J, Häffner H and Blatt R 2003 The coherence of qubits based on single Ca$^+$ ions *J. Phys. B: At. Mol. Opt. Phys.* **36** 623

[37] Acton M, Brickman K-A, Haljan P C, Lee P J, Deslauriers L and Monroe C 2006 Near-perfect simultaneous measurement of a qubit register *Quantum Inform. Comput.* **6** 465–82

[38] Blinov B B, Leibfried D, Monroe C and Wineland D J 2004 Quantum computing with trapped ion hyperfine qubits *Quantum Inform. Process.* **2** 45

[39] Diedrich F, Berquist J C, Itano W M and Wineland D J 1989 Laser cooling to the zero-point energy of motion *Phys. Rev. Lett.* **62** 403–6

[40] Deslauriers L, Haljan P C, Lee P J, Brickman K-A, Blinov B B, Madsen M J and Monroe C 2004 Zero-point cooling and low heating of trapped Cd ions *Phys. Rev.* A **70** 043408

[41] Blinov B, Deslauriers L, Lee P, Madsen M, Miller R and Monroe C 2002 Sympathetic cooling of trapped Cd$^+$ isotopes *Phys. Rev.* A **65** 040304

[42] Barrett M D *et al* 2003 Sympathetic cooling of $^9Be^+$ and $^{24}Mg^+$ for quantum logic *Phys. Rev.* A **68** 042302

[43] Rohde H, Gulde S T, Roos C F, Barton P A, Leibfried D, Eschner J, Schmidt-Kaler F and Blatt R 2001 Sympathetic ground-state cooling and coherent manipulation with two-ion crystals *J. Opt. B: Quantum Semiclass. Opt.* **3** S34–S41

[44] Hensinger W, Olmschenk S, Stick D, Hucul D, Yeo M, Acton M, Deslauriers L, Monroe C and Rabchuk J 2006 T-junction ion trap array for two-dimensional ion shuttling, storage, and manipulation *Appl. Phys. Lett.* **88** 034101

[45] Wineland D J, Monroe C, Itano W M, Leibfried D, King B E and Meekhof D M 1998 Experimental issues in coherent

quantum-state manipulation of trapped atomic ions *J. Res. Natl Inst. Stand. Technol.* **103** 259–328

[46] Kielpinski D, Monroe C and Wineland D J 2002 Architecture for a large-scale ion-trap quantum computer *Nature* **417** 709–11

[47] Leibfried D, Knill E, Ospelkaus C and Wineland D J 2007 Transport quantum logic gates for trapped ions *Phys. Rev. A (At. Mol. Opt. Phys.)* **76** 032324

[48] Sakurai J J 1993 *Modern Quantum Mechanics* (Reading, MA: Addison-Wesley)

[49] Metcalf H J and van der Straten P 2002 *Laser Cooling and Trapping* (Berlin: Springer)

[50] Lee P J, Brickman K A, Deslauriers L, Haljan P C, Duan L M and Monroe C 2005 Phase control of trapped ion quantum gates *J. Opt. B: Quantum Semiclass. Opt.* **7** S371–83

[51] Ozeri R *et al* 2005 Hyperfine coherence in the presence of spontaneous photon scattering *Phys. Rev. Lett.* **95** 030403

[52] Milburn G J, Schneider S and James D F V 2000 Ion trap quantum computing with warm ions *Fortschr. Phys.* **48** 9–11, 801–10

[53] Mølmer K and Sørensen A 1999 Multiparticle entanglement of hot trapped ions *Phys. Rev. Lett.* **82** 1835–8

[54] Leibfried D *et al* 2003 Experimental demonstration of a robust, high-fidelity geometric two ion-qubit phase gate *Nature* **422** 412–5

[55] Haljan P C, Brickman K-A, Deslauriers L, Lee P J and Monroe C 2005 Spin-dependent forces on trapped ions for phase-stable quantum gates and motional Schrödinger cat states *Phys. Rev. Lett.* **94** 153602

[56] Haljan P C, Lee P J, Brickman K-A, Acton M, Deslauriers L and Monroe C 2005 Entanglement of trapped-ion clock states *Phys. Rev. A (At. Mol. Opt. Phys.)* **72** 062316

[57] Turchette Q A *et al* 2000 Heating of trapped ions from the quantum ground state *Phys. Rev.* A **61** 063418

[58] Deslauriers L, Olmschenk S, Stick D, Hensinger W K, Sterk J and Monroe C 2006 Scaling and suppression of anomalous heating in ion traps *Phys. Rev. Lett.* **97** 103007

[59] Labaziewicz J, Ge Y, Antohi P, Leibrandt D, Brown K R and Chuang I L 2008 Suppression of heating rates in cryogenic surface-electrode ion traps *Phys. Rev. Lett.* **100** 013001

[60] Stick D, Hensinger W, Olmschenk S, Madsen M, Schwab K and Monroe C 2006 Ion trap in a semiconductor chip *Nature Phys.* **2** 36–9

[61] Seidelin S *et al* 2006 Microfabricated surface-electrode ion trap for scalable quantum information processing *Phys. Rev. Lett.* **96** 253003

[62] Grover L 1997 Quantum mechanics helps in searching for a needle in a haystack *Phys. Rev. Lett.* **79** 325

[63] Schmidt-Kaler F, Häffner H, Riebe M, Gulde S, Lancaster G P T, Deuschle T, Becher C, Roos C F, Eschner J and Blatt R 2003 Realization of the Cirac–Zoller controlled-not quantum gate *Nature* **422** 408–11

[64] Gulde S, Riebe M, Lancaster G P T, Becher C, Eschner J, Häffner H, Schmidt-Kaler F, Chuang I L and Blatt R 2003 Implementation of the Deutsch–Jozsa algorithm on an ion-trap quantum computer *Nature* **421** 48–50

[65] Riebe M *et al* 2004 Deterministic quantum teleportation with atoms *Nature* **429** 734–7

[66] Barrett M D *et al* 2004 Deterministic quantum teleportation of atomic qubits *Nature* **429** 737–9

[67] Chiaverini J *et al* 2005 Implementation of the semiclassical quantum Fourier transform in a scalable system *Science* **308** 997–1000

[68] Griffiths R B and Niu C-S 1996 Semiclassical Fourier transform for quantum computation *Phys. Rev. Lett.* **76** 3228–31

[69] Schaetz T, Barrett M D, Leibfried D, Chiaverini J, Britton J, Itano W M, Jost J D, Langer C and Wineland D J 2004 Quantum dense coding with atomic qubits *Phys. Rev. Lett.* **93** 040505

[70] Brassard G 1997 Searching a quantum phone book *Science* **275** 627–8

[71] Grover L K 1998 A framework for fast quantum mechanical algorithms *Proc. 20th ACM Symp. Theory of Computing (Dallas, TX, 24–26 May 1998)* (New York: ACM) pp 53–62

[72] Brickman K-A, Haljan P, Lee P J, Acton M, Deslauriers L and Monroe C 2005 Implementation of Grover's quantum search algorithm in a scalable system *Phys. Rev.* A **72** 050306(R)

[73] Boyer M, Brassard G, Hoyer P and Tapp A 1998 Tight bounds of quantum searching *Fortschr. Phys.* **46** 493

[74] Leibfried D *et al* 2005 Creation of a six-atom 'Schrödinger cat' state *Nature* **438** 639

[75] Häffner H *et al* 2005 Scalable multiparticle entanglement of trapped ions *Nature* **438** 643–6

[76] Benhelm J, Kirchmair G, Roos C F and Blatt R 2008 Towards fault-tolerant quantum computing with trapped ions *Nature Phys.* **4** 463–6

[77] Monz T, Kim K, Hansel W, Riebe M, Villar A S, Schindler P, Chwalla M, Hennrich M and Blatt R 2009 Realization of the quantum toffoli gate with trapped ions *Phys. Rev. Lett.* **102** 040501

[78] Ospelkaus C, Langer C E, Amini J M, Brown K R, Leibfried D and Wineland D J 2008 Trapped-ion quantum logic gates based on oscillating magnetic fields *Phys. Rev. Lett.* **101** 090502

[79] Kim J, Pau S, Ma Z, McLellan H R, Gates J V, Kornblit A, Slusher R E, Jopson R M, Kang I and Dinu M 2005 System design for large-scale ion trap quantum information processor *Quant. Inform. Comput.* **5** 515

[80] Kim J and Kim C 2009 Integrated optical approach to trapped ion quantum computation *Quantum Inform. Comput.* **9** 181

[81] Luo L, Hayes D, Manning T A, Matsukevich D N, Maunz P, Olmschenk S, Sterk J D and Monroe C 2009 Protocols and techniques for a scalable atom-photon quantum network *Fortschr. Phys.* **57** 1133

[82] Knill E 2005 Quantum computing with realistically noisy devices *Nature* **434** 39

[83] Raussendorf R and Harrington J 2007 Fault-tolerant quantum computation with high threshold in two dimensions *Phys. Rev. Lett.* **98** 190504

[84] Reichardt B W 2004 Improved ancilla preparation scheme increases fault-tolerant threshold arXiv:quant-ph/0406025v1

[85] Chiaverini J *et al* 2004 Realization of quantum error correction *Nature* **432** 602

[86] Schmidt P O, Rosenband T, Langer C, Itano W M, Berquist J C and Wineland D J 2005 Spectroscopy using quantum logic *Science* **309** 749

[87] Rosenband T *et al* 2008 Frequency ratio of Al$^+$ and Hg$^+$ single-ion optical clocks; metrology at the 17th decimal place *Science* **319** 1808

[88] Lloyd S 1996 Universal quantum simulators *Science* **273** 1073

[89] Friedenauer A, Schmitz H, Glueckert J T, Porras D and Schaetz T 2008 Simulating a quantum magnet with trapped ions *Nature Phys.* **4** 757

[90] Kim K, Chang M-S, Islam R, Korenblit S, Duan L-M and Monroe C 2009 Entanglement and tunable spin–spin couplings between trapped ions using multiple transverse modes *Phys. Rev. Lett.* **103** 120502